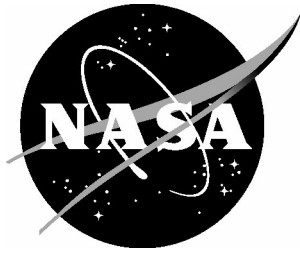# Transport Equation Based Wall Distance Computations Aimed at Flows With Time-Dependent Geometry

Paul G. Tucker
University of Warwick, Coventry, UK

Christopher L. Rumsey, Robert E. Bartels, and Robert T. Biedron
Langley Research Center, Hampton, Virginia

Since its founding, NASA has been dedicated to the advancement of aeronautics and space science. The NASA Scientific and Technical Information (STI) Program Office plays a key part in helping NASA maintain this important role.

The NASA STI Program Office is operated by Langley Research Center, the lead center for NASA's scientific and technical information. The NASA STI Program Office provides access to the NASA STI Database, the largest collection of aeronautical and space science STI in the world. The Program Office is also NASA's institutional mechanism for disseminating the results of its research and development activities. These results are published by NASA in the NASA STI Report Series, which includes the following report types:

- TECHNICAL PUBLICATION. Reports of completed research or a major significant phase of research that present the results of NASA programs and include extensive data or theoretical analysis. Includes compilations of significant scientific and technical data and information deemed to be of continuing reference value. NASA counterpart of peer-reviewed formal professional papers, but having less stringent limitations on manuscript length and extent of graphic presentations.

- TECHNICAL MEMORANDUM. Scientific and technical findings that are preliminary or of specialized interest, e.g., quick release reports, working papers, and bibliographies that contain minimal annotation. Does not contain extensive analysis.

- CONTRACTOR REPORT. Scientific and technical findings by NASA-sponsored contractors and grantees.

- CONFERENCE PUBLICATION. Collected papers from scientific and technical conferences, symposia, seminars, or other meetings sponsored or co-sponsored by NASA.

- SPECIAL PUBLICATION. Scientific, technical, or historical information from NASA programs, projects, and missions, often concerned with subjects having substantial public interest.

- TECHNICAL TRANSLATION. English-language translations of foreign scientific and technical material pertinent to NASA's mission.

Specialized services that complement the STI Program Office's diverse offerings include creating custom thesauri, building customized databases, organizing and publishing research results ... even providing videos.

For more information about the NASA STI Program Office, see the following:

- Access the NASA STI Program Home Page at *http://www.sti.nasa.gov*

- E-mail your question via the Internet to help@sti.nasa.gov

- Fax your question to the NASA STI Help Desk at (301) 621-0134

- Phone the NASA STI Help Desk at (301) 621-0390

- Write to:
  NASA STI Help Desk
  NASA Center for AeroSpace Information
  7121 Standard Drive
  Hanover, MD 21076-1320

NASA/TM-2003-212680
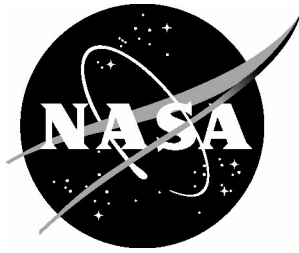
Transport Equation Based Wall Distance Computations Aimed at Flows With Time-Dependent Geometry

Paul G. Tucker
University of Warwick, Coventry, UK

Christopher L. Rumsey, Robert E. Bartels, and Robert T. Biedron
Langley Research Center, Hampton, Virginia

December 2003

Available from:

CONTENTS

ABSTRACT
Eikonal, Hamilton-Jacobi and Poisson equations can be used for economical nearest wall distance computation and modification. Economical computations may be especially useful for aeroelastic and adaptive grid problems for which the grid deforms, and the nearest wall distance needs to be repeatedly computed. Modifications are directed at remedying turbulence model defects. For complex grid structures, implementation of the Eikonal and Hamilton-Jacobi approaches is not straightforward. This prohibits their use in industrial CFD solvers. However, both the Eikonal and Hamilton-Jacobi equations can be written in advection and advection-diffusion forms, respectively. These, like the Poisson's Laplacian, are commonly occurring industrial CFD solver elements. Use of the NASA CFL3D code to solve the Eikonal and Hamilton-Jacobi equations in advective-based forms is explored. The advection-based distance equations are found to have robust convergence. Geometries studied include single and two element airfoils, wing body and double delta configurations along with a complex electronics system. It is shown that for Eikonal accuracy, upwind metric differences are required. The Poisson approach is found effective and, since it does not require offset metric evaluations, easiest to implement. The sensitivity of flow solutions to wall distance assumptions is explored. Generally, results are not greatly affected by wall distance traits.

ABBREVIATIONS

MF   Marching front approach (used to speed up GGS)

GGS   Global Gauss-Seidel

NNS   Nearest normal surface search

NSS   Nearest surface search

2D   Two dimensional

3D   Three dimensional

1. INTRODUCTION

Normal wall distances, *d*, are still a necessary parameter in a range of key turbulence models (see Fares and Schroder (2002)), Detached Eddy Simulation (DES) type approaches (Strelets (2001)) and also peripheral applications incorporating additional solution physics (Osher and Sethian (1988) and Tucker (2001)). Also, near wall iso-values can be used to convert, for example, tetrahedral meshes into hybrid ones. The lines of constant *d* form the basis of a body fitted grid (see Sethian (1999)). Far field *d* contours can also be used as a rapid means of evaluating computational interfaces on unstructured overset meshes having relative movements (Nakahasi and Togashi (2000)). Surprisingly, for highly optimised RANS/URANS (Unsteady Reynolds Averaged Navier-Stokes) solvers, the effort in calculating *d* can be a significant fraction of the total solution time. For example, even with Cray C90 class computers and time invariant meshes it can take 3 hours just to compute *d* (Wigton (1998)). Because of *d* evaluation expense, in some codes dangerous approximations are made. The following are given by Spalart (2000):

a) computing distances down grid lines and not allowing for grid non-orthogonality;
b) computing '*d*' as the distance between a field point and the nearest wall grid point and
c) in multiblock solutions ascertaining '*d*' on a purely block wise basis ignoring the possibility that the nearest wall distance might be associated with another block.

The latter can create large inaccuracies and also non-smooth *d* distributions that can inhibit convergence. In relation to point (c), Spalart (2000) notes for overset grids the situation can arise where the same point in space has different equations.

Clearly the listed practices will give mostly inexact distances (or even multiple distances) $\tilde{d}$. However, the careful modification of *d* to some $\tilde{d}$ can remedy turbulence model deficiencies or extend modeling potential (Secundov et al. (2001)). For example, $\tilde{d} \gg d$ can remedy excessive sharp convex feature turbulence model influence (see Fares and Schroder (2002) and Tucker (2003)). For corners or bodies/surfaces in close proximity, there is an increased multiple surface turbulence damping effect (Mompean et al. (1996), Launder et al. (1975)). This effect can be modeled by setting $\tilde{d} < d$.

Search procedures, integral approaches and differential equations can be used to find *d*. Crude searches require $O(n_v n_s)$ operations where n_s and n_v correspond to the number of surface and internal node points. Wigton (1998) and Boger (2001) present more efficient procedures needing $O(n_v \sqrt{n_s})$ and $O(n_v \log n_s)$ operations, respectively. Wigton's approach searches for nearest surfaces, i.e. it is a nearest surface search (NSS). Strictly, turbulence models are developed with the nearest normal surface (NNS) in mind. However, *d* fields for this are non-smooth. Integral *d* computation approaches are described in Boger (2001) and Launder et al. (1975). For complex geometries they are difficult to apply. Hence, the focus here is on differential equation based methods suitable for vector and parallel computers.

There are several differential equation based methods. The level set method of Osher and Sethian (1988) solves a differential time (*t*) evolution equation

($\partial\phi/\partial t + |\nabla\phi| = \Gamma\nabla^2\phi$ and $\Gamma \to 0$). The d field is evaluated in $O(n_v^4)$ operations from the times at which the dependent variable reaches a set level. Motivated by solution expense, Sethian (1999) casts the level set approach into a boundary value framework. The Eikonal equation below is used.

$$|\nabla\phi| = 1 \qquad\qquad (1.1)$$

This can be solved in $O(n_v \log n_v)$ operations. The Equation (1.1) dependent variable, ϕ, models propagating front first arrival times. The right hand side implies the front has unit velocity, i.e. there is some velocity field with $|\mathbf{U}| = 1$. Fares and Schroder (2002) essentially solve an Eikonal type equation for ϕ^{-1} adding a modified Laplacian to give $\tilde{d}$. The Eikonal equation with a Laplacian, as below, is a Hamilton-Jacobi equation.

$$|\nabla\phi| = f(\phi)\nabla^2\phi \qquad\qquad (1.2)$$

Spalding (see Tucker (2003)) approximately reconstructs d from solution of a Poisson equation ($\nabla^2\phi = -1$). The $d(\phi)$ reconstruction involves an auxiliary analytically derived equation. An efficient Poisson equation solver typically scales as $O(n_v \log n_v)$. The Eikonal, unlike the Poisson equation (see Sethian (1999), Tsai (2002) and Tucker (2003)), is challenging to code. This is especially the case for unstructured grids (see Sethian and Vladimirsky (2002)). Hence its implementation in established industrial CFD solvers presents a significant time investment and hence cost. Therefore, here use of an Eikonal equation form that is amenable to general geometry CFD code implementation is explored. The form is reminiscent of the Euler/Navier-Stokes equations (the key equations modeled in CFD solvers). Also, since the Poisson d method is easy to implement in such codes this approach is further studied. For the current work, as the base CFD solver for the wall distance studies, the NASA CFL3D program (see Krist et al. (1998)) is primarily used.

Operation counts show differential approaches can be significantly faster than search procedures. However, for fixed mesh problems it is unusual for the search procedure to contribute significantly to the total CFD solution cost. Nonetheless, for the increasingly common flow solutions where the mesh deforms and sometimes also refines (perhaps with varying cell numbers) the repeated search cost becomes highly significant (see Boger (2001)). Then, differential approaches, which can make easy, safe use of previous d estimates, become especially attractive. The new d approaches presented here are best viewed in this moving mesh context. However, most of the examples chosen involve stationary meshes. These primarily test the robustness and convergence traits and so seem appropriate. The approaches considered are now outlined.

2. GOVERNING *d* EQUATIONS

The Eikonal is an exact *d* equation. When defining the vector

$$\mathbf{U} = \nabla\phi \ , \tag{2.1}$$

it can be rewritten in the following advection analogous form

$$\mathbf{U} \bullet \nabla\phi = 1 . \tag{2.2}$$

The vector $\mathbf{U}$ corresponds to the front propagation velocity implied in the Eikonal equation and so again $|\mathbf{U}| = 1$. As noted by Fares and Schroder (2002) and Tucker (2003), Laplacians can be used to modify *d* and so remedy turbulence model defects. Motivated by this, the following advection-diffusion *d* equation is also considered

$$\mathbf{U} \bullet \nabla\phi = 1 + \Gamma(\phi)\nabla^2\phi \tag{2.3}$$

Equation (2.3) when solved with (2.1) gives a Hamilton-Jacobi equation solution. The positive function $\Gamma(\phi)$ is discussed later. Since $(\nabla\phi)^2 = \nabla \bullet (\phi\nabla\phi) - \phi\nabla^2\phi$ and $\mathbf{U} = \nabla\phi$, the following conservative form of (2.3) is also possible

$$\nabla \bullet (\phi\mathbf{U}) = 1 + \Gamma^*\nabla^2\phi \tag{2.4}$$

where

$$\Gamma^* = (\Gamma + \phi) \tag{2.5}$$

Along different lines, substitution of the Poisson based ϕ distribution arising from solving Equation (2.3) with $\mathbf{U} = 0$ and $\Gamma = 1$ into

$$d = -\sqrt{\sum_{j=1,3}\left(\frac{\partial\phi}{\partial x_j}\right)^2} \pm \sqrt{\sum_{j=1,3}\left(\frac{\partial\phi}{\partial x_j}\right)^2 + 2\phi} \tag{2.6}$$

also gives distances (see Tucker (2003)). The derivation of (2.6) assumes extensive (infinite) coordinates in the non-normal wall directions. Hence, unlike the Eikonal, *d* is only accurate close to walls. However, turbulence models only need *d* accurate close to walls.

In summary, Equation (2.2) gives an Eikonal equation solution. However, to distinguish an Equation (2.2) solution from the direct solution of the Eikonal Equation (1.1), Equation (2.2) solutions are referred to as advective *d* equation solutions. Equation (2.3, 2.4) solutions are distinguished from direct Equation (1.2) Hamilton-Jacobi solutions by calling them advection-diffusion *d* equation solutions. Equation (2.6) solutions are referred to here as Poisson *d* equation solutions.

Laplacian form and role

Near a fine convex feature (for example a wire), accurate distances are needed for theoretical correctness, so $\tilde{d} = d$. However, to prevent excessive far field influence $\tilde{d} \gg d$ can be required (see Fares and Schroder (2002) and Tucker (2003)). Adjacent to a convex feature $\Gamma\nabla^2 d \gg 0$. Therefore, the positive Laplacian inclusion in (2.3) has the desired effect of enlarging/exaggerating $d(=\phi)$. Motivated by dimensional homogeneity, the need that as $d \to 0$, $\tilde{d} = d$ but $\nabla^2\phi \to \infty$ suggests

$$\Gamma = \varepsilon d \qquad\qquad\qquad (2.7)$$

where ε is a constant. Clearly more 'aggressive' functions than (2.7) (e.g. $\Gamma = \varepsilon(-1 + e^d)$) are possible but these are not explored. The Eikonal equation with $f(\phi)\nabla^2\phi$ is, as noted earlier, a Hamilton-Jacobi equation.

At concave corners $\nabla^2 d < 0$, hence $\tilde{d} \ll d$. Therefore, with the Laplacian, the damping effects of 'extra' walls, discussed earlier, is naturally accounted for. At a d maximum, say for example at the center line of a channel, again $\nabla^2 d < 0$. This is sensible (see Fares and Schroder (2002)), since again it will naturally model the damping effect of the two adjacent walls. Eikonal and hence Equation (2.3) distances will generally be discontinuous in gradient (e.g., this occurs where fronts effectively propagating from different walls collide). Therefore, the $\nabla^2 d$ term smoothing has the potential to enhance convergence.

3. NUMERICAL METHODS

Here, the numerical methods to solve Equations (2.2-2.4) are described. The Poisson based method is not covered here. For numerical details on this method see Tucker (1998). Equations (2.2-2.4) can be solved on Cartesian, general curvilinear and unstructured grids. For curvilinear grids they must be transformed using the chain rule for differential calculus in, say, a (ξ, η) system. When solving in this, metric terms (M) such as $\xi_x (= \partial\xi/\partial x)$, η_x, ξ_y, and η_y must be evaluated. This aspect will be discussed more later. Diffusive terms in Equations (2.3-2.4) are discretized using second order central differences. The advective derivatives in Equations (2.2-2.4) are discretized, just considering an x-coordinate direction for example, using the following 1st order upwind type of approximation

$$\frac{\partial\phi}{\partial x} \approx n_{i-1}\Delta_{i-1,j,k}\phi + n_{i+1}\Delta_{i+1,j,k}\phi \tag{3.1}$$

where

$$\Delta_{i-1,j,k}\phi = \frac{\phi_i - \phi_{i-1}}{\Delta x_{i-1}}, \quad \Delta_{i+1,j,k}\phi = \frac{\phi_{i+1} - \phi_i}{\Delta x_{i+1}} \tag{3.2}$$

and

$n_{i-1} = 1$ for $u_{i-1} > -u_{i+1}$ and $u_{i-1} > 0$ else $n_{i-1} = 0$; and
$n_{i+1} = 1$ for $-u_{i+1} > u_{i-1}$ and $-u_{i+1} > 0$ else $n_{i+1} = 0$.

The propagation velocities in the above are simply evaluated using Equations (2.1), where, for example

$$u_{i-1} = \frac{\phi_i - \phi_{i-1}}{\Delta x_{i-1}}, \quad u_{i+1} = \frac{\phi_{i+1} - \phi_i}{\Delta x_{i+1}} \tag{3.3}$$

Setting $\Gamma = 0$ in (2.3) shows that the conservation form of the d equation has a Laplacian. Here the view is taken that the discretized *conservation* form of the equation is used (Equation (2.4)). However, for optimal solution of the advective d equation form (using an advancing front approach), the extra Laplacian $\phi\nabla^2\phi$ must be ignored. The approximation of neglecting $\phi\nabla^2\phi$ could be considered as solving the non-conservation Equation (2.2) with the alternative approximation that

$$u_i = n_{i-1}u_{i-1} + n_{i+1}u_{i+1} \tag{3.4}$$

The above equation corresponds to using offset difference-based velocity components. These would correspond to those needed in the conservative Equation (2.4) form. Either viewpoint has no great accuracy implications. Where d needs to be accurate for turbulence modeling, $\phi\nabla^2\phi \to 0$. Numerical tests confirm the validity of the above arguments.

Metric Discretization
As shown in Tucker (2003), for strongly stretched grids the metric terms (M) must be carefully discretized. In CFL3D, for the *i* index 'direction' M_{i-1} and M_{i+1} metrics are first evaluated. The latter, for example, involves geometric data at the i and i+1 grid points. These M_{i-1} and M_{i+1} difference-based constructs are then, as with most CFD codes, averaged to give a single M_i value to be used in the discretised transport equations. However, as shown in Tucker (2003), for strongly expanding near wall grid spacings this results in *d* overestimations. The simple remedy used by Tucker (2003) is the following metric formulation

$$M_i = n_{i-1}M_{i-1} + n_{i+1}M_{i+1} \tag{3.5}$$

The standard CFL3D implementation corresponds to $n_{i-1} = n_{i+1} = 1/2$ in the above.

Stabilizing Measures
To ensure stable solution of the transport based *d* equations, velocity clipping and diagonal dominance enhancement have been used. Both use the observation that, in 2D, the exact **U** field should satisfy

$$R_u = \left| u_{i,j}^2 + v_{i,j}^2 - 1 \right| = 0 \tag{3.6}$$

where *u* and *v* are velocity components in the *x* and *y* directions, respectively. Therefore, to improve diagonal dominance, R_u and $R_u\phi_i$ are added to both the discretized equation matrix diagonals and source term, respectively. Based on Equation (3.6), the following velocity clipping is also used

$$\left| u_{i,j} \right| \le 1, \quad \left| v_{i,j} \right| \le 1 \tag{3.7}$$

The Eikonal equation does not permit a backwards front movement (see Sethain (1999)). The implication of this restriction is that if in (2.3), for example, $\Gamma\nabla^2\phi < -1$ a theoretical violation occurs (the sign of the Equation (2.3) right hand side gives the front propagation direction). Hence, when solving the advection-diffusion form of the *d* equation, the Laplacian of Equation (2.3) (*L*) is modified to

$$L = \max\left[-C, \Gamma\nabla^2\phi\right] \tag{3.8}$$

where $0 \le C \le 1$. Here, *C* = 1 is used. This is the limit for theoretical correctness. Since anti-diffusion is associated with instability, use of (3.8) should be viewed as a stability measure.

As a further stability measure, under-relaxation is used either through the following $\phi = (1-\alpha)\phi^{old} + \alpha\phi^{new}$ (where α is an under-relaxation factor and the 'new' and 'old' superscripts indicate iterative states), or through the use of a pseudo time term.

When solving the Eikonal equation, evaluation of the discretized matrix coefficients for each grid point needs around 160 operations. The advective Eikonal equation form (Equation (3.6)) needs 90 operations, but then iteration is also required (i.e. Equations

(2.1) and (2.3) must be contained in some iterative loop). Therefore, the key efficiency issue is the number of iterations N typically required. This is discussed later.

Simultaneous equation solution
Here, either essentially crude global Gauss-Seidel (GGS) type iterations or a marching front (MF) approach is used. The essence of the MF approach is illustrated using Fig. 1. In this, a 'wire' is represented on a Cartesian grid using a single node point. Points surrounding this are considered to be either seed, trial, or those to be later solved. These points are labelled through the marker variable ns with the following respective values 2, 1 and 0. To start, a seed (or multiple seeds) point is defined. The advective d equation is applied N times (until convergence) to assign this point a d value. As noted earlier, the N iterations involve repeated application of the discretized d equation followed by substitution of the result in Equation (2.1) to find $\mathbf{U}$. The seed is represented in Frame (I) by the closed symbol. The advective d equation is then used with Equation (2.1) for all immediate seed neighbors (trial points). These $ns = 1$ points are shown as open symbols. As shown in Frame (II), the trial point with the minimum d is taken as the next seed. Now, for this point, $ns = 2$. Then, as shown in Frame (III), d for all immediate neighbors to the new seed (for which $ns \neq 2$) are calculated. Hence the next seed point location is found. Frames (IV) and (V) show subsequent development stages for a clockwise moving circular front. In summary the procedure is as follows:

a) Define a seed point;
b) Iteratively solve for d at immediate neighbors to the seed (trial points) and
c) Make the trial point with the minimum d the next seed and return to (a).

This procedure is continued until $ns = 2$ for all points in Ω or a smaller domain/extent $\tilde{\Omega}$ identified by the Fig. 1 dotted line (many turbulence models and DES only need d to a maximum of about $1/3^{\text{rd}}$ the boundary layer thickness). In a practical system, all surface adjacent points can be taken as seeds, and what is called an 'active front' is produced. For best efficiency a heap-sort procedure is required. This procedure has not been incorporated as part of this work. When a Laplacian is included, the MF approach can only be used to obtain an initial guess. Cleary, based on operation counts, $N < 2$ is needed for the advective d equation to match the Eikonal's efficiency.

Initial/Starting Conditions
For the advection analogous d equations, $1 < \phi < \infty$ in Ω is found to be adequate. However, for MF solutions, $\phi \rightarrow \infty$ is used. When using the MF approach to give a DES distance field, $\phi = C_{DES}\Delta_i$ is used where $\Delta_i = \max(\Delta x, \Delta y, \Delta z)$ is the DES 'filter' control. The d computation naturally stops when $d = C_{DES}\Delta_i$. For the Poisson approach, $\phi \approx 0$ is adequate.

Boundary Conditions
Boundary conditions on the domain boundaries are now described. At solid walls the following Dirichlet condition is applied

$$\phi = 0 \tag{3.9}$$

At flow/far field boundaries

$$\frac{\partial \phi}{\partial n} = 0 \qquad\qquad\qquad (3.10)$$

can be used, where n is the boundary normal co-ordinate. However, if Ω is sufficiently large, (3.9) makes a stable, most computationally economical far field boundary condition. It is especially preferred for the Poisson method, for which it gives much faster convergence.

4. DISCUSSION OF RESULTS

The following geometries are considered:

   (a) Flat plate;
   (b) Electronics system;
   (c) Single element airfoils (NACA 4412 and 0012);
   (d) Wing body;
   (e) Wing flap and
   (f) Double delta.

For cases (c-f) where d 'error' values are given, these are relative to NSS distances. Of course the NSS cannot be regarded as exact wall distances but they do serve as a useful reference point. Negative errors correspond to a d over-prediction. Unless otherwise stated, flow solutions use the Spalart and Allmaras (1994) (SA) turbulence model. This probably has the most extreme d requirements of most standard turbulence models. It needs d accurate for around 1/3rd the boundary layer thickness. Hence it is a good candidate for d modeling tests. Quoted CPU times are for a 300 MHz SGI Origin.

Flat Plate(Case (a))

To test advective d equation solution method performance, a flat plate is considered. Other d methods are not considered for this case. The plate is positioned at $y = 0$ in a 2D square domain Ω with sides of unit length. Equation (3.10) is used at the 'far-field' boundaries. Essentially, the two Fig. 2 grids are considered. The mildly sinusoidal function, distorted Frame (a) mesh is used as a basis for exploring the effect of grid expansion on accuracy. To do this the y direction grid positions are strongly expanded by raising them to some power k. The revised grid locations are at y^k, where y is for the initial grid. In Frame (a) $k = 1$. The Frame (b) grid also uses $k = 1$. However, the frequency and amplitude of the sinusoidal disturbance is much higher. This grid is intended to severely test the accuracy and robustness of the advective d equation solution process. Table 1 gives % d errors for different k with offset (Equation (3.5)) and centered metrics. The parameter in the second column (α_y) is a geometric grid expansion factor estimate.

k	α_y	% d Error	
		Offset metrics	Centered metrics
1.1	1.1	0.48	1.53
1.5	1.7	0.99	8.25
2	2.6	3.15	15.0

Table 1. % d errors with offset and centered metrics.

Clearly, with centered differences and larger k values, serious errors arise. This is perhaps not surprising. As noted by Roache (1976), for accurate flow solutions $\alpha_y < 1.3$ is needed. Also, the front propagation nature of the advective d equations makes errors additive. Furthermore, centered differences are inconsistent with a propagating front problem. Fig. 3 plots predicted against actual distances (y) at x=0.5. Frame (a)

is for the Fig. 2a grid with $k=2.6$. Frame (b) is for the Fig. 2b grid. The full lines give the exact solutions. The circles are for offset metrics and the triangles for centered metrics. The Frame (a) d over-prediction arising from centered metrics is clear and consistent with the Eikonal equation observations of Tucker (2003). Frame (b) shows that (with offset metrics) even with an extremely distorted grid, reasonable distances can be obtained.

Fig. 4 shows strongly distorted grid (Fig. 2b) velocity data. Frames (a) and (b) give $|\mathbf{U}|$ contours and $\mathbf{U}$ vectors, respectively. Considering the poor grid form, the velocity magnitudes and direction are surprisingly good. Fig. 5 gives a plot of log (R_u) (see Equation (3.6)) against GGS iterations for the strongly distorted grid. An under-relaxation factor, $\alpha = 0.7$, is used. Through its monotonic nature, the plot reflects the stable convergence.

Complex electronics system (Case (b))
Next, the Fig. 6 geometry is considered. For this case Poisson, NNS, Eikonal, advective and advection-diffusion d solutions are made. Fig. 7 gives x-y and y-z plane views of the Cartesian blocked off grid used as part of Case (b) studies. Initially some convergence studies are made using a coarsened Fig. 7 grid structure with just 20,000 points. Fig. 8 uses a histogram to indicate advective d equation MF convergence. It shows the percentage of grid points needing various N values for an under-relaxation parameter (α) of 0.6. Generally $N = 4$. Therefore, since the advective d equation operation count is 45% less than the Eikonal, the former has roughly twice the computational cost. However, clearly, for non-stationary grids N will greatly drop. Also, as previously noted, for unstructured grids and industrial CFD solvers the advective d equation is a more practical option than the Eikonal. Fig. 9 plots R_u against N for GGS with $\alpha = 0.2$, 0.6 and 0.8. Clearly, for GGS, $\alpha = 0.8$ gives best convergence. This high value reflects the advective d procedure's convergence robustness. Table 2 gives MF to GGS total iteration ratios and MF scheme N values for different α. MF convergence is taken to occur when $R_u < 0.001$. For GGS this convergence level could not be achieved, R_u being around 30% higher.

α	MF/GGS	N (MF)
0.2	0.14	9
0.4	0.17	5
0.6	0.26	4
0.8	0.47	5

Table 2. Iteration ratios and N.

Table 2 shows the MF approach significantly reduces the number of iterations at each grid point. Also, pleasingly, N is not an excessively strong function of α.

The Laplacian in the advection-diffusion form of the d equation (Equation (2.3)) had little convergence influence. Even with $\varepsilon = 10$, the $\alpha = 0.6$ convergence is virtually identical. It can therefore perhaps be concluded that the advective d equation is quite stable, not needing any additional stabilizing diffusion.

Fig. 10 gives circa mid x-y plane $\mathbf{U}$ and d error data for an advective d equation solution. Correctly, the Frame (a) vectors are surface normal. In corners, shock

analogous features can be found. At 'convex' corners these are the expansion type. Correctly, the frame (b) |**U**| contours are close to unity having an average value of 1.004 (using a 0.001 % error in R_u as a basis for convergence). Frame (c) gives the % difference in d relative to a NNS field. The major discrepancies are seen to be around the 'shock' features and right hand side flow outlets.

Fig. 11 gives x-y plane d contours. Frames (a-e) are for the NNS, Poisson, Eikonal, advective, and advection-diffusion solutions, respectively. The NNS contours are, as they should be, discontinuous. When using the CFL3D NSS procedure, sharp convex feature distances become similar to those for the Fig. 11 Eikonal/advective d equation results. For illustrative purposes, the advection-diffusion d solution (Frame (e)) uses an extremely large $\varepsilon = 10$ value in Equation (2.7). Such a large value would (unless a function with a more rapid near wall decay than (2.7) is used) contaminate d accuracy and hence could not be used as part of a practical CFD solution. The Poisson result naturally gives strong corner contour rounding. Correctly, the Eikonal and advective d equation solutions are virtually identical. Their distance traits appear as a compromise between those of the NNS and Poisson methods. Over the complete domain the average d deviation (relative to the search) for the Eikonal, Poisson, and advective equation approaches is 4.4, 17.1, and 4.8%, respectively. These differences appear significant. However, in the regions of greatest importance, near walls and away from corners, all the approaches give very similar distances. To see this, it is worth comparing Eikonal d solutions with the zonal k-ε /k-l Poisson based d predictions of Tucker and Pan (2002). In this work, velocities and turbulence intensities are compared with measurements over six profiles. The average solution difference over these profiles, for the two d approaches, is just 2.8%. The discrepancy between the flow solutions and measurements is around 25%. Fig. 12 gives zoomed in views of d contours around regions A and B of the Frame (e) $\varepsilon = 10$ solution. The Fig. 12 views show that the Laplacian has the effect of exaggerating d around sharp convex features (contour lines bias themselves to corners). Around concave features the reverse occurs. As noted earlier, both traits can be beneficial, remedying turbulence model defects.

Fig. 13 shows the RANS/LES interface for a DES solution. This was computed using the advective d equation and MF approach. To bring the interface away from the surface, so it can be seen more clearly, the Fig. 7 cell density is halved and $C_{DES} = 1.3$. This is twice the standard C_{DES} value. The advective approach with the MF solution naturally gives a DES 'd' field. It avoids wasted computational effort by terminating at the RANS/LES interface. The non-uniform nature of the interface reflects a DES complex grid deficiency. DES implies the interface location is at $d = C_{DES}$ max($\Delta x, \Delta y, \Delta z$). From studying the Fig. 7 grid, it is clear this interface will be non-smooth.

Fig. 14 plots d against y for the Poisson, search, and advective d solutions. The lines are located around the mid x and z locations of the system. The full, long and short dashed lines correspond to the search, advective, and Poisson approaches, respectively. As can be seen, away from walls the Poisson distances differ significantly from those for the other approaches.

Single element airfoils (Cases (c))

In this section, results for both NACA 4412 and 0012 airfoils are considered. The Poisson, advective *d*, NSS, and NNS procedures are compared. The NACA 4412 angle of attack is fixed at 13.87°, $M = 0.2$ and, $Re = 1.52 \text{ x } 10^6$ based on chord. For the NACA 0012, the mean angle of attack is 4.86°, $M = 0.6$ and $Re = 4.8 \text{ x } 10^6$. The wing has a forced pitching oscillation of 50.32 Hz with an amplitude of 2.44° (AGARD Case 3). Wall distances are computed using modified CFL3D solver elements. These modifications include use of upwind metric differences. For the NACA 4412 and 0012, comparisons are made with the measurements of Coles and Wadock (1979), and Landon (1982), respectively.

Fig. 15 shows the single block 'C' and 3 zone overset grids used for the NACA 4412 studies. Both involve around 25,000 grid nodes. Fig. 16 shows circa 33,000 cell NACA 0012 'C' grids at around the minimum (2.6°) and maximum (7.2°) pitch angles. With the grid re-distribution used (see Bartels (2000)) the near wall grid tends to move with the surface. Hence, for this simple case, the near surface *d* values should alter little.

First, we consider the NACA 4412 case. Fig. 17 shows *d* contours representing in the following respective frames the: (a) NSS; (b) NNS; (c) advective equation; (d) Poisson and (e) overset grid Poisson results. Frames (a)-(d) represent results on the 'C' grid, and Frame (e) represents results on the 3-zone overset grid. Overset Poisson solutions are made for the complete domain Ω, and also just for the surface mapping block region ($\tilde{\Omega}$). Obviously, the latter solution, shown in Frame (e), is most computationally efficient. At the $\tilde{\Omega}$ boundaries the Dirichlet condition $\phi = 0$ is used. Perhaps the most strikingly different *d* contours are those representing the nearest NNS shown in Frame (b).

Fig. 18 gives $y^+ < 400$, *d* error histograms. The error is defined using the equation below

$$Error = 100(\frac{d_{NNS} - d}{d_{NNS}}) \qquad\qquad (4.1)$$

where d_{NNS} is the distance from the nearest surface search. The *d* without the subscript in Equation (4.1) is the distance field for which the error is being evaluated. Frame (a) is for the advective *d* equation with upwind metrics. The average 'error' is 0.5%. Without upwind metrics *d* is overestimated by an average of 6%. Frame (b) is for the overset grid Poisson solution using $\tilde{\Omega}$. Although not shown by the error histograms, the average *d* error for the Poisson is significantly higher than that for the advective equation. The 'C' grid Poisson error histogram looks very similar to that for Frame (b).

Fig. 19 gives a zoomed in view of trailing edge region Poisson *d* 'error' contours. As can be seen, a key *d* overestimation zone is the sharp convex trailing edge geometry region. This overestimation zone is potentially desirable. As can be seen later, distance overestimation can remedy a turbulence model defect.

Fig. 20 gives **U** vectors for the advective d equation. Frames (a) and (b) are **U** vectors for the 'C' and overset grids, respectively. The vectors correctly show surface normal **U** components. The magnitude of these is close to unity.

Table 3 gives NACA 4412 lift coefficients (C_L) and drag coefficients (C_D) for the advective, NSS, NNS, and Poisson methods.

	C_L	C_D
Advective	1.704	0.03466
NSS	1.698	0.03496
NNS	1.712	0.03514
Poisson	1.713	0.03543

Table 3. NACA 4412 C_L and C_D's for different d fields.

Some minor differences are evident. Their nature is partly clarified in Fig. 21, giving surface C_p (pressure coefficient) curves. The full, dashed and dot-dashed lines are for the Poisson, NSS, and NNS approaches, respectively. The symbols give measured data. Differences can only clearly be seen when zooming in close to the trailing edge region. The advective d equation results are not shown. However, they do not fall outside the curve envelope for the other methods shown in Fig. 21.

Fig. 22 plots top airfoil surface streamwise mean fluid velocity against the cross-stream coordinate. The plot is made near the trailing edge at $x/c = 0.953$ (c is the airfoil chord and $x/c = 0$ corresponds to the leading edge). This is the only region where any velocity discrepancies can be discerned. The velocity is normalized by the free stream value U_o. The line styles are the same as in Fig. 21. Velocity differences for the different d fields are small, confined to the trailing edge region and of no great consequence.

The SA model's turbulence destruction terms can be excessively active around sharp convex features (see Tucker (2003)). Fig. 23 gives SA trailing edge region turbulent viscosity (μ_t) contours for the NSS (Frame (a)), NNS (Frame (b)), and Poisson (Frame (c)) approaches. The large NNS distances in the region $x/c > 1$ greatly reduce the modeled turbulence destruction. As noted earlier the Poisson method also has this trait. The reduced turbulence destruction for the NNS and Poisson approaches relative to the NSS is evident in Fig. 23. Fig. 24 compares Poisson predicted trailing edge Reynolds stress contours with those inferred from measurements. Frames (a), (b), and (c) give the following respective components: $\overline{u'u'}/U_o^2$, $\overline{u'v'}/U_o^2$ and $\overline{v'v'}/U_0^2$. For predictions these values are approximated from $\overline{u'_i u'_j} = 2\mu_t S_{ij}/\rho$ where S_{ij} is strain rate and ρ fluid density. Contour levels have been chosen to match those identified for the hot wire measurements. As might be expected, due to the simpler nature of the SA model (for which the predicted stresses have very limited meaning) and vagaries of contour plotting the correspondence between the predictions and measurements is not high. However, both sets of results suggest higher turbulence energy zones for $\overline{u'u'}/U_o^2$ and $\overline{u'v'}/U_o^2$.

Fig. 25 plots $\overline{u'u'}/U_o^2$ against y/c at $x/c = 1.1$. The full, dot-dashed, and dashed lines are for the Poisson, NNS, and NSS approaches, respectively. Symbols give measured values. Clearly, the NNS and Poisson approaches, having larger $x/c > 1$ d fields and hence less modeled destruction, give larger $\overline{u'u'}/U_o^2$ values. The advective d results, not shown in the graph, are similar to those for the NSS. Table 4 gives integrated/averaged % normal stress intensity values, $(u'/U_o)_{ave}$, for $-0.05 < y/c < 0.028$. As suggested by Fig. 25, the Poisson and NNS approaches yield a higher peak that is somewhat closer to the measurements. Again, as noted for Fig. 24, SA has limited accuracy when predicting $\overline{u'u'}/U_o^2$. Hence, the above results should be partly viewed as giving quantative information on the sensitivity of turbulence statistics to wall distance assumptions.

	$(u'/U_o)_{ave}\%$
Measured	3.10
Poisson	2.90
NNS	2.89
Advective	2.77
NSS	2.77

Table 4. Average $x/c = 1.1$
normal intensity values.

Clearly, for the current case, turbulence intensities downstream of the airfoil have insignificant influence on the parameters of interest in an aeronautical design context. However, for multiple element airfoils it is not inconceivable that more significant solution differences could arise. These can be caused by a peak in modeled turbulence energy convecting close to the center of the leading edge of a downstream element. Small changes in the turbulence energy peak's position could give rise to different solutions (Spalart (2002)).

Next, we present results for the pitching NACA 0012 case. Fig. 26 compares NACA 0012 lift and moment coefficient (C_M) measurements, represented by symbols, with predictions. The full lines give an NSS d solution with a non-deforming grid that rotates with the airfoil. The long dashed and dotted lines are for deforming grid NSS and Poisson d distribution solutions, respectively. Importantly, the NSS solution uses a time invariant d distribution taken from the non-deforming grid case. Frames (a) and (b) give lift and moment coefficient data, respectively. For time accurate solutions, at least 10 sub-iterations per time step are required. Streamwise Courant numbers are around unity. The similarity of the lines suggests, as might be expected for this simple geometry, that the scheme used for the grid redistribution keeps the surface grid form quasi-constant with time. Hence it is very similar to that for the fixed mesh case. Therefore, the major differences between the fixed and deforming mesh results can most probably be attributed to discretization errors arising through the mesh movement and not wall distance differences. As might be expected, the Poisson

equation approach needs little convergence effort. However, this is to a large extent due to the relatively low levels of grid deformation for this case. Nonetheless, the Poisson approach is found to require a factor of around 2.25 less computing time than the search. Also, GGS solver iterations comprise about a factor of 1/100 of the total Poisson cost. Therefore, with large grid movements the Poisson method is likely to be very efficient.

Wing body (Case (d))
For this wing body case the angle of attack is 2.87^o, $M = 0.802$ and $Re = 13.1 \times 10^6$ based on the wing chord. The single block grid shown in Fig. 27 involves around 0.9 million cells. For this case the Poisson, advective d, and NSS d procedures are used. Fig. 28 gives the $y^+ < 400$-region 'error' histogram for the advective d and Poisson methods. The average 'errors' are 3.13% and 3.14%, respectively. The Poisson's tendency to over predict d is evident in the histograms. For this more complex geometry case, unlike the NACA 4412 results, the average differences between lift and drag coefficients for the different d fields is lower. This can be seen in Table 5, giving C_L and C_D values for the different d fields.

	C_L	C_D
Advective	0.6633	0.04839
NSS	0.6632	0.04855
Poisson	0.6635	0.04842

Table 5. Case (d) C_L and
C_D's for different d fields.

Wing Flap (Case (e))
The Case (e) wing and flap angles are 2° and 40°, respectively. The wing-flap gap is 0.6% of the wing chord (c). The Reynolds number, based on c, is 23×10^6 and $M=0.18$. Part of the 10-block, approximately 0.9 million-cell grid is shown in Fig. 29. For this case the Poisson, NSS, and advective d procedures are tested.

In Fig. 30, d contours for the NSS (Frame (a)), advective (Frame (b)), and Poisson (Frame (c)) methods are qualitatively compared. As can be seen, near walls the contours are similar. For the Poisson method, away from walls there is some unsightly d behaviour. This, as noted in Tucker (2003), is due to significant levels of block interface grid non-orthogonality (the CFL3D solver assumes grid orthogonality) and the use of backward differences in Equation (2.6). The Poisson equation's trait of overestimating trailing edge d values is evident. Fig. 31 plots the d equation residual log against the number of GGS type iterations. As can be seen, the residual can be reduced to machine round-off. Fig. 32 presents **U** vectors for the advective equation d solution. Frame (b) gives a zoomed in view of the flap nose region. Correctly, the vectors are surface normal. Magnitudes are close to unity.

Fig. 33 gives $y^+ < 400$ 'error' histograms. Frame (a) is for the upwind metric advective equation. Frame (b) is for the Poisson. The average Frame (a) 'error' is 2.09%. The grid is highly stretched. Therefore, with centered metrics this error rises to 10.36%. The Poisson equation has a 1% error. This low Poisson error, relative to the advective equation seems to contradict the histogram evidence. This suggests the advective d equation has some large 'errors' at just a very few points.   Clearly, the Frame (a) advective equation 'error' distribution has the least spread. For the Poisson

method (see Frame (b)), it can be seen there is a slight tendency to overpredict d. As can be inferred from Table 6, Poisson method lift and drag coefficients are within 0.05% of those for the NSS procedure. For the advective d equation, the deviation is a little greater but not that significant.

	C_L	C_D
Advective	2.815	0.0582
NSS	2.810	0.0584
Poisson	2.811	0.0584

Table 6. Case (e) C_L and
C_D's for different d fields.

Double delta wing (Case (f))
For this double delta case the advective d, NNS, and Poisson methods are used. The angle of attack is 6°, $M = 0.96$ and $Re = 2.2$ x 10^6. A key motivation for this case was aeroelasticity studies made as part of Boeing's sonic cruiser development. Fig. 34 shows initial and severely deformed aeroelasticity calculation surface grids. These use 1.2 million cells. The meshes are far more severely deformed than for a realistic engineering calculation. Extreme plunging generates the deformations. They are intended to produce severely deformed cells to strongly test the robustness of differential equation based d approaches. Frames (a, b) of Fig. 34 are 3D views. Frames (c, d) are 2D y-z plane views. For moving mesh performance studies two approximately equi-spaced deflection increments between the Fig. 34 extremes are considered.

Fig. 35 gives advective d equation **U** component vectors and d contours in three z-y planes. Correctly, the Frame (a) vectors are surface normal. The Frame (b) contours wrap around the object surface. This suggests their potential grid generation use. Fig. 36 shows the advective d and Poisson equation residual drops against iteration for a stationary mesh solution using the Fig. 34a,c grids. Mesh sequencing with three grid levels is used. The abrupt gradient changes generally signify where a finer mesh has been moved to. Considering the crude GGS type solver, convergence is adequate, requiring around 20 and 40 sec of CPU time for the Poisson and advective d equations, respectively. The NSS needs 57 sec. In an aero-elasticity calculation, this constitutes around 20% of the time step cost. When solving the Poisson and advective d equations over the two equi-spaced deflection increments, just a fraction of a second of CPU time is required. This is mostly because of the effectiveness of the spring analogy surface grid redistribution procedure (near surface cell relative positions hardly change) and also because in a non-stationary grid mode the differential equations have a good initial guess for the iterative solution.

Fig. 37 gives $y^+ < 400$ 'error' histograms. Frame (a) is for the upwind metric advective equation. Frame (b) is for the Poisson. The average Frame (a) 'error' is 3.27%. With centered metrics this error rises to around 7%. The average Poisson error is 2.67%. Encouragingly, the Case (f) lift and drag coefficients for the Poisson method are within 0.03 and 0.06% of those for the NSS procedure.

Table 7 summarises the Poisson and advective equation 'errors' for cases (b-f). From this it is clear that the theoretically exact advective d equation is not always more

accurate than the approximate Poisson. This is most probably because the latter is more numerically benign. The hyperbolic advective d equation does have the advantage that it can be solved in the DES and zonal RANS compatible MF mode (also, it can be used for other, non-turbulence related, CFD purposes). However, a consequence of its hyperbolic form is that upwind metrics are required and also d errors are additive (addition occurs in the front propagation direction). The elliptic Poisson does not suffer with this additive d error trait. As discussed in Section 2, the advective equation can be cast in a Hamilton-Jacobi form. This gives the potential to control convex and concave feature d distributions, and so remedy turbulence model defects. Although the Poisson method offers no explicit convex/concave feature d control, its natural traits in such regions appear helpful. It is difficult to conclude which method is best. This is especially the case since their use is purpose dependent. For example, the Poisson approach is totally unsuitable for evaluating far-field computational interfaces on overset meshes as needed for the approach of Nakahashi and Togashi (2000). It is also worth remembering that 'error' values given here are relative to the NSS approach, and that this cannot be regarded as providing a perfect d field.

Case	% 'Error'	
	Advective	Poisson
(b)	4.8	17
(c)	0.5	3
(d)	3.1	3.1
(e)	2.1	1
(f)	3.3	2.7

Table 7. Case (b-f) d error summary.

5. CONCLUSIONS

Advection and advection-diffusion forms of the Eikonal and Hamilton-Jacobi wall distance (d) equations have been presented. These have been studied because of their relatively easy potential implementation in industrial CFD solvers. Mostly, use of the NASA CFL3D CFD program to solve the advective-based d forms was explored. The advection based d equations were found to have robust convergence. Geometries studied included single and two-element airfoils, wing body and double delta configurations, along with a complex electronics system. It was shown that for Eikonal accuracy, offset metric differences are required. A simple, approximate, Poisson-equation-based distance approach was found effective and, since it did not require offset metric evaluations, easiest to implement. The sensitivity of flow solutions to d assumptions was explored. Generally, results were not greatly affected by wall distance traits. However, the use of, for example, nearest surface search distances was found to reduce downstream trailing edge intensities by around 4.5%. Results suggest that for stationary meshes the advective d equation has about twice the computational cost of the Eikonal, but for moving meshes this difference greatly decreases. However, CFL3D's hybrid TFI/spring analogy grid redistribution scheme maintains near wall relative grid positions well. Consequently, for non-stationary grids, differential equation based d approaches were not greatly challenged.

6. ACKNOWLEDGEMENTS

REFERENCES

R. E. Bartels, Mesh strategies for accurate computation of unsteady spoiler and aeroelastic problems, J. of Aircraft, Vol. 37, No. 3, pp. 521-525 (2000)

D. A. Boger, Efficient method for calculating wall proximity, AIAA Journal, Vol. 39, No. 12, pp. 2404-2406 (2001)

D. Coles and A. J. Wadcock, Flying hot-wire study of flow past an NACA 4412 airfoil at maximum lift, AIAA J., Vol. 17, No. 4, pp. 321-329 (1979)

E. Fares and W. Schroder, A differential equation to determine the wall distance, Int. J. for Numerical Methods in Fluids, Vol. 39, pp 743-762 (2002)

S. L. Krist, R. T. Biedron and C. L. Rumsey, CFL3D user's manual (version 5.0), NASA/TM-1998-208444, 1998.

R. H. Landon, Compendium of unsteady aerodynamic measurements, "NACA 0012. Oscillatory and transient pitching," Data set 3, AGARD-R-702 (1982)

B. E. Launder, G. J. Reece and W. Rodi, Progress in the development of a Reynolds-stress turbulence closure, J. Fluid Mech., Vol. 68, Part 3, pp. 537-566 (1975)

G. Mompean, S. Gavrilakis, L. Machiels and M. O. Deville, On predicting the turbulence-induced secondary flows using non-linear k-ε models, Phys. Fluids, Vol. 8, No. 7, pp. 1856-1868 (1996)

K. Nakahashi and F. Togashi, Unstructured overset grid method for flow simulation of complex multiple body problems, ICAS 2000 Congress, Paper No. ICAS 0263 (2000)

S. Osher and J. A. Sethain, Fronts propagating with curvature dependent speed: Algorithms based on Hamilton-Jacobi formulation, J. Comput. Phys., Vol. 79 , pp. 12-49 (1988)

P. J. Roache (1976) Computational fluid dynamics, Hermosa, Albuquerque, N. M.

N. Secundov, M. Kh. Strelets, A. K. Travin, Generalisation of vt-92 turbulence model for shear-free and stagnation point flows, Journal of Fluids Engineering, March, Vol. 123, pp. 111-15 (2001)

J. A. Sethain, Level set methods and fast marching methods, Cambridge University Press (1999)

J. A Sethian, A. Vladimirsky, Fast methods for the Eikonal and related Hamilton-Jacobi equations on unstructured grids, Proceedings National Academy of Science, USA, May 23, 2000, Vol. 97, No. 11, pp. 5699-5703 (2000)

P. R. Spalart, Trends in turbulence model treatments, AIAA Paper 2000-2306 (2000)

P. R. Spalart, The Boeing Company, Personal communication (2002)

M. Strelets, Detached eddy simulation of massively separated flows, AIAA Paper 2001-0879 (2001)

P. R. Spalart and S. R. Allmaras, A one-equation turbulence model for aerodynamic flows, La Rech. Aerospatiale, Vol. 1, pp. 5-21 (1994)

Y. R. Tsai, Rapid and accurate computation of the distance function using grids, Journal of Computational Physics, Vol. 178, pp.175-195 (2002)

P. G. Tucker, Assessment of geometric multilevel convergence and a wall distance method for flows with multiple internal boundaries, Applied Mathematical Modeling, Vol. 22, pp. 293-311 (1998)

P. G. Tucker, Differential equation based wall distance computation for DES and RANS J. of Computational Physics, Vol. 190, Issue 1, 1st September, pp. 229-248 (2003)

P. G. Tucker, Computation of particle and scalar transport for complex geometry turbulent flows, ASME J. of Fluids Engineering, Vol. 123, June, pp. 372-381 (2001)

P. G. Tucker and Z. Pan, URANS computations for a complex internal isothermal flow, Comp. Meths in Applied Mechanics and Engineering, Vol. 190, pp. 2893-2907 (2001)

L. B. Wigton, Optimizing CFD codes and algorithms for use on Cray computers, Frontiers of Computational Fluid Dynamics (Editors D. A. Caughey and M. M. Hafez), Chapter 16, pp. 1-15, World Scientific Publishing Co. Pte. Ltd. ISBN 981-02-3707-3 (1998)
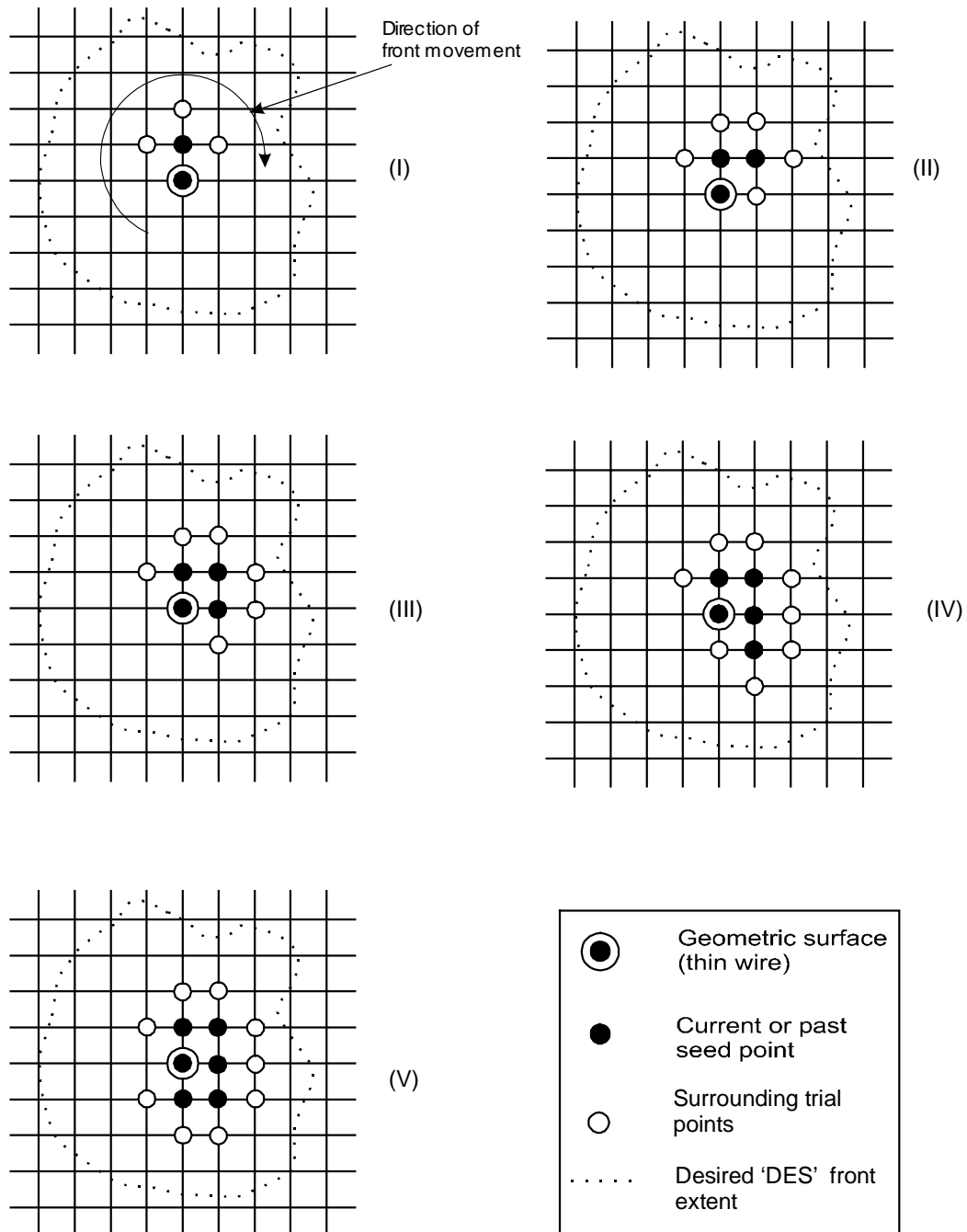
Fig. 1. Solution using MF approach with a single seed point.
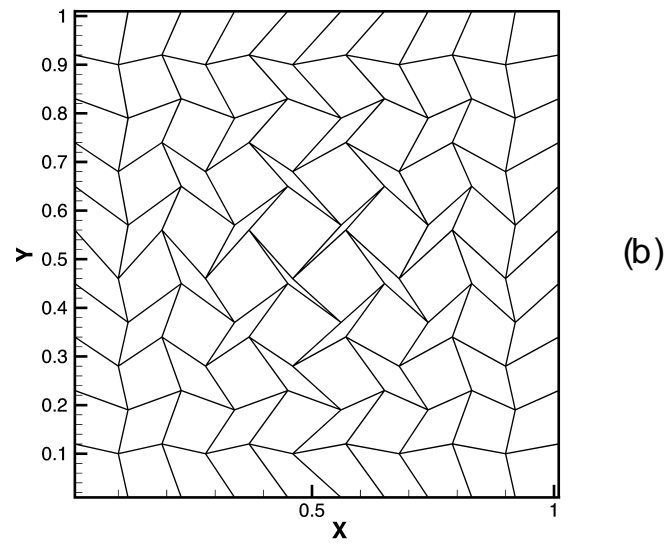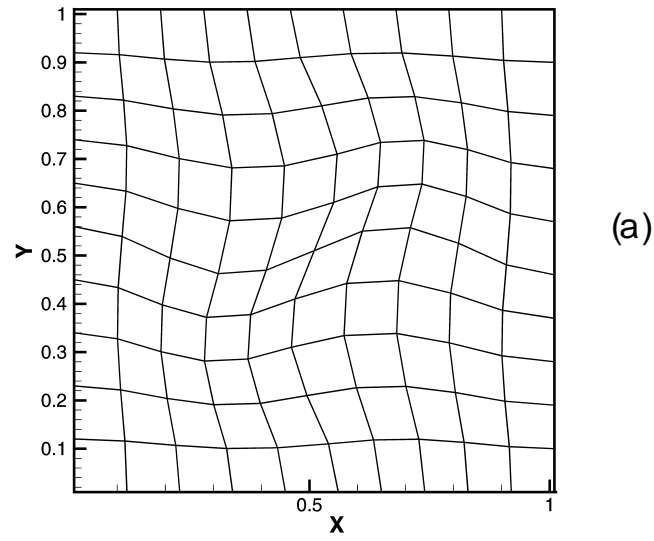
Fig. 2. Case (a) grids: (a) mildly distorted and (b) strongly distorted.
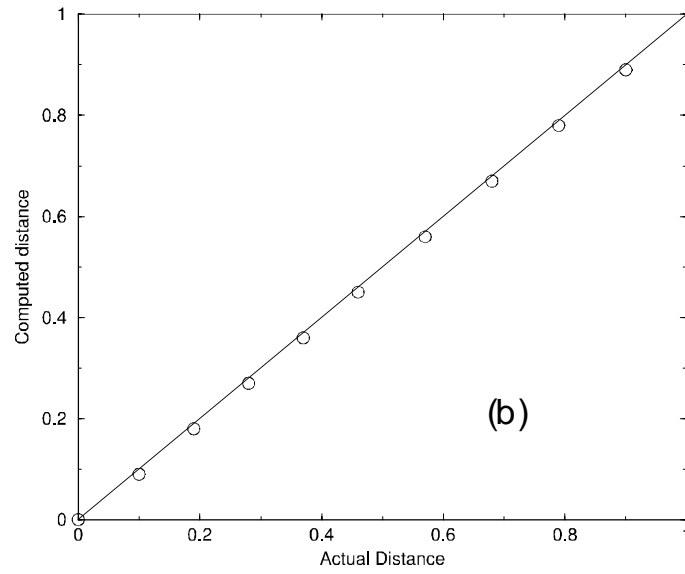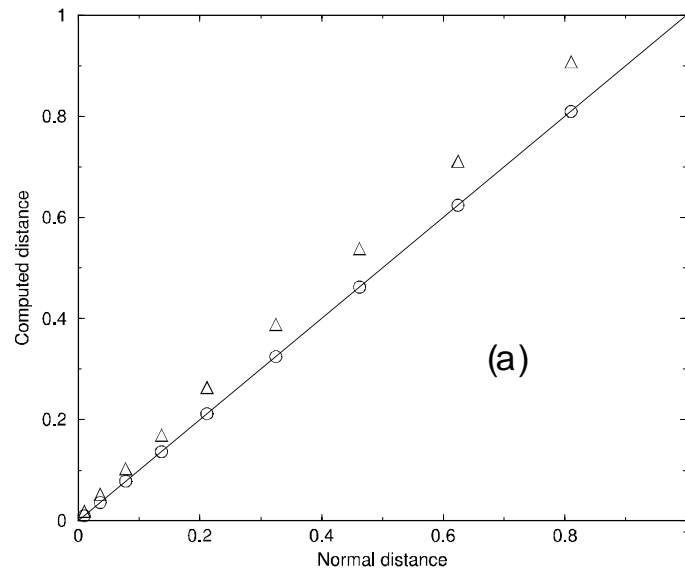
Fig. 3. Predicted against actual distances (*y*) at *x*=0.5 for flat plate:
(a) strongly stretched grid and (b) strongly distorted
(——exact solution, O offset metrics, Δ centered metrics).
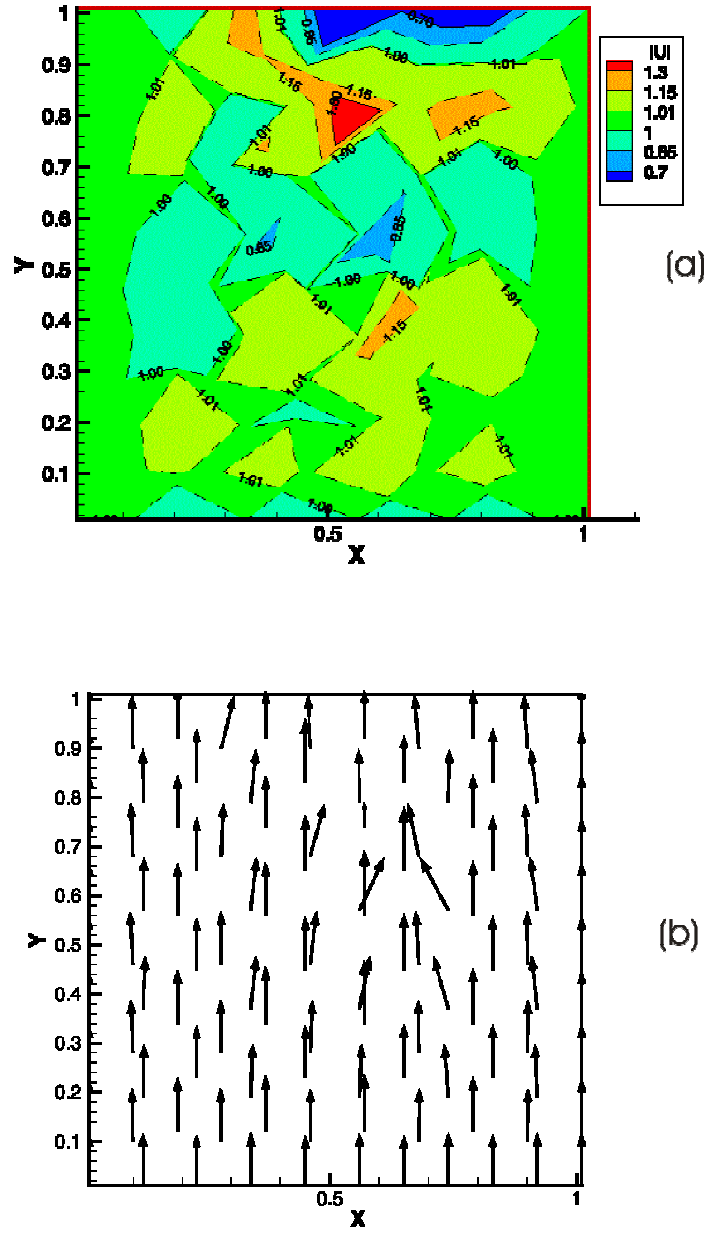
Fig. 4. Velocity data for strongly distorted grid: (a) |U| and (b) U vectors.
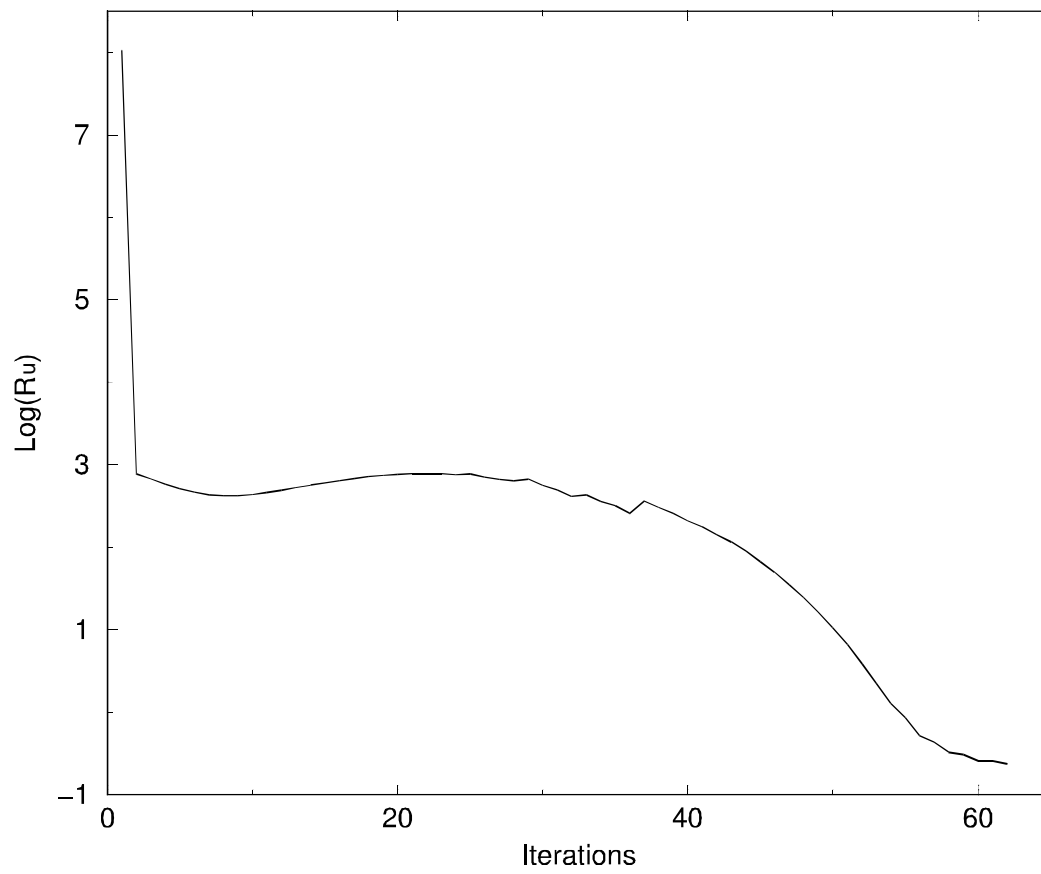
Fig. 5. Plot of log(R_u) against GGS iterations for strongly distorted grid.
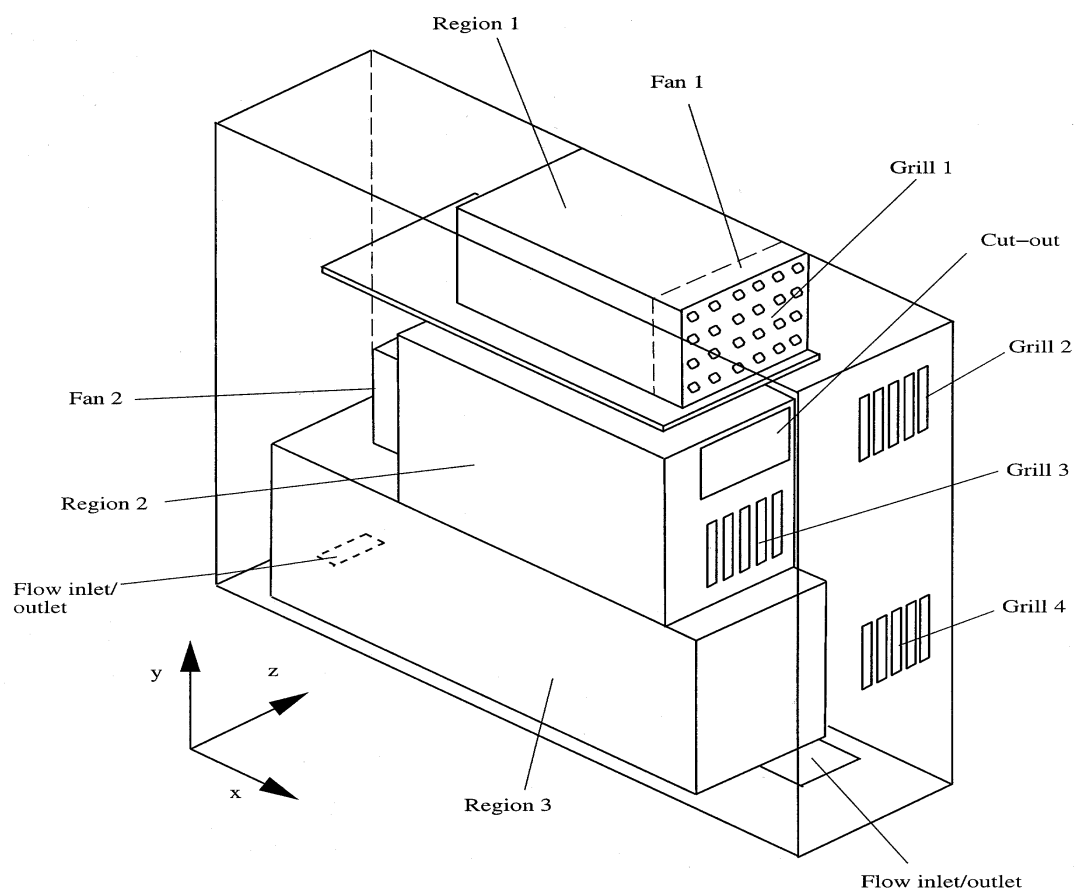
Fig. 6. Schematic of the Case (b) geometry.
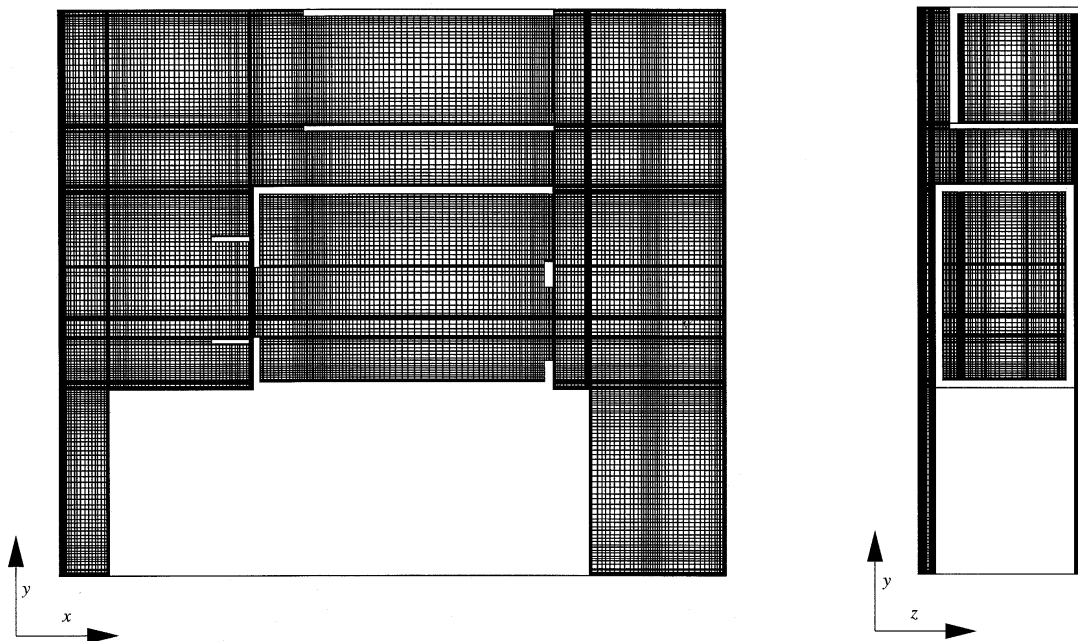
Fig. 7. Case (b) (Electronic system) mid-plane grid structures:
(a) *x-y* plane and (b) *z-y* plane.
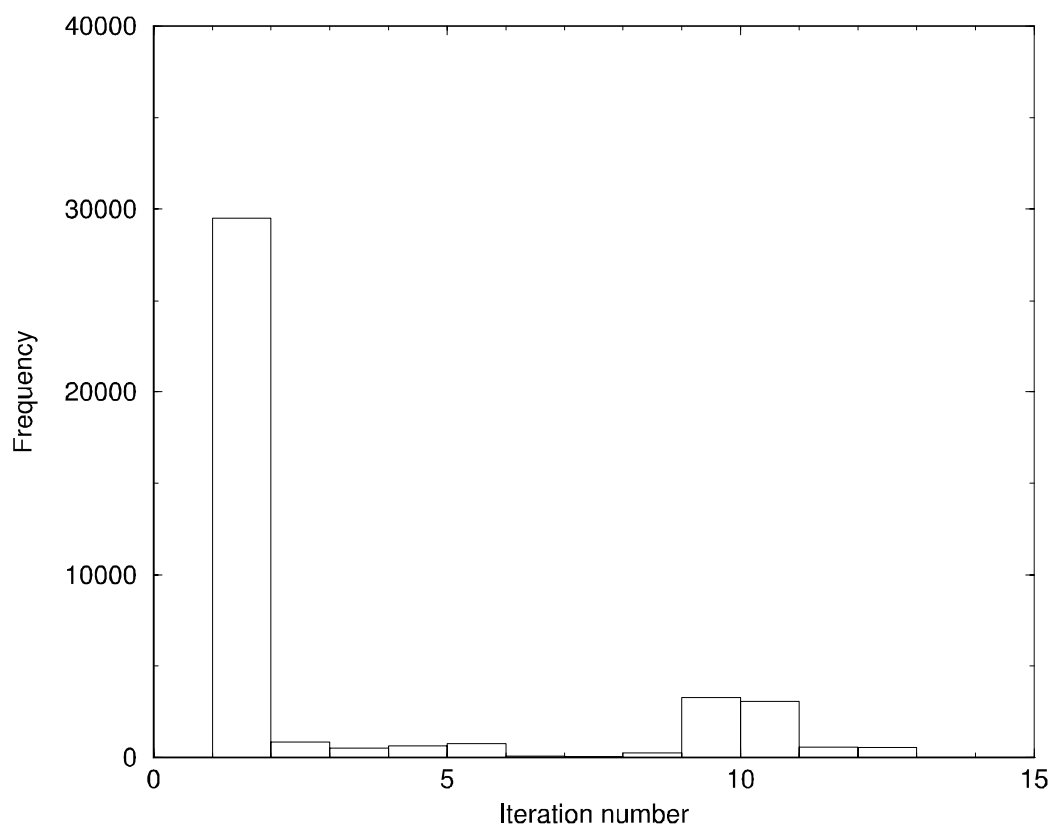
Fig. 8. Histogram indicating the % of grid points needing various N values for MF convergence.
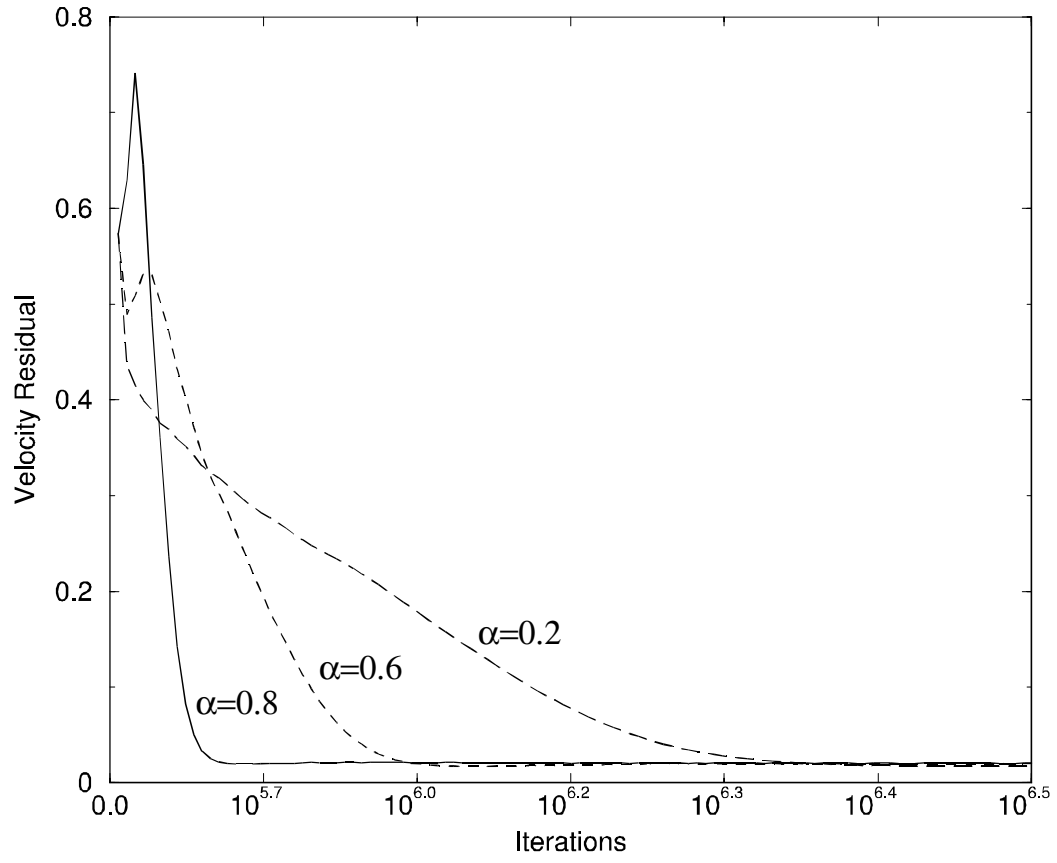
Fig. 9. Case (b) (electronics system) plot of R_u against iterations for GGS solver.

(a)

1.100
1.033
0.967
0.900

(b)

1.000

−1.000

(c)
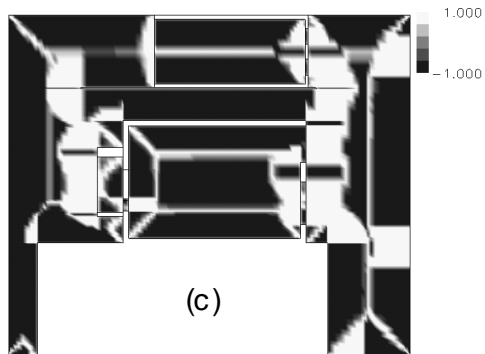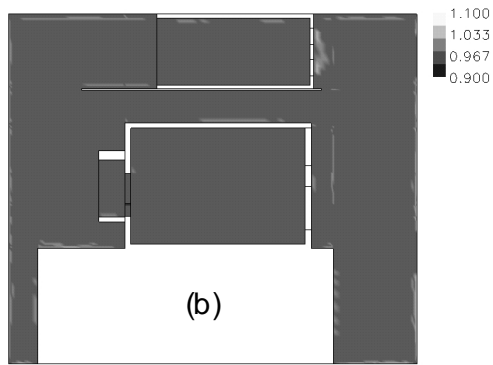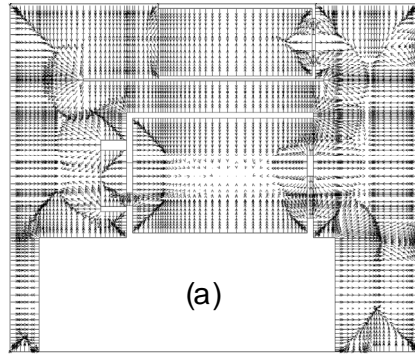
Fig. 10. Case (b) mid *x-y* plane **U** and *d* error data for an advective *d* equation solution:
(a) **U** vectors; (b) |**U**| contours and (c) % 'error.'
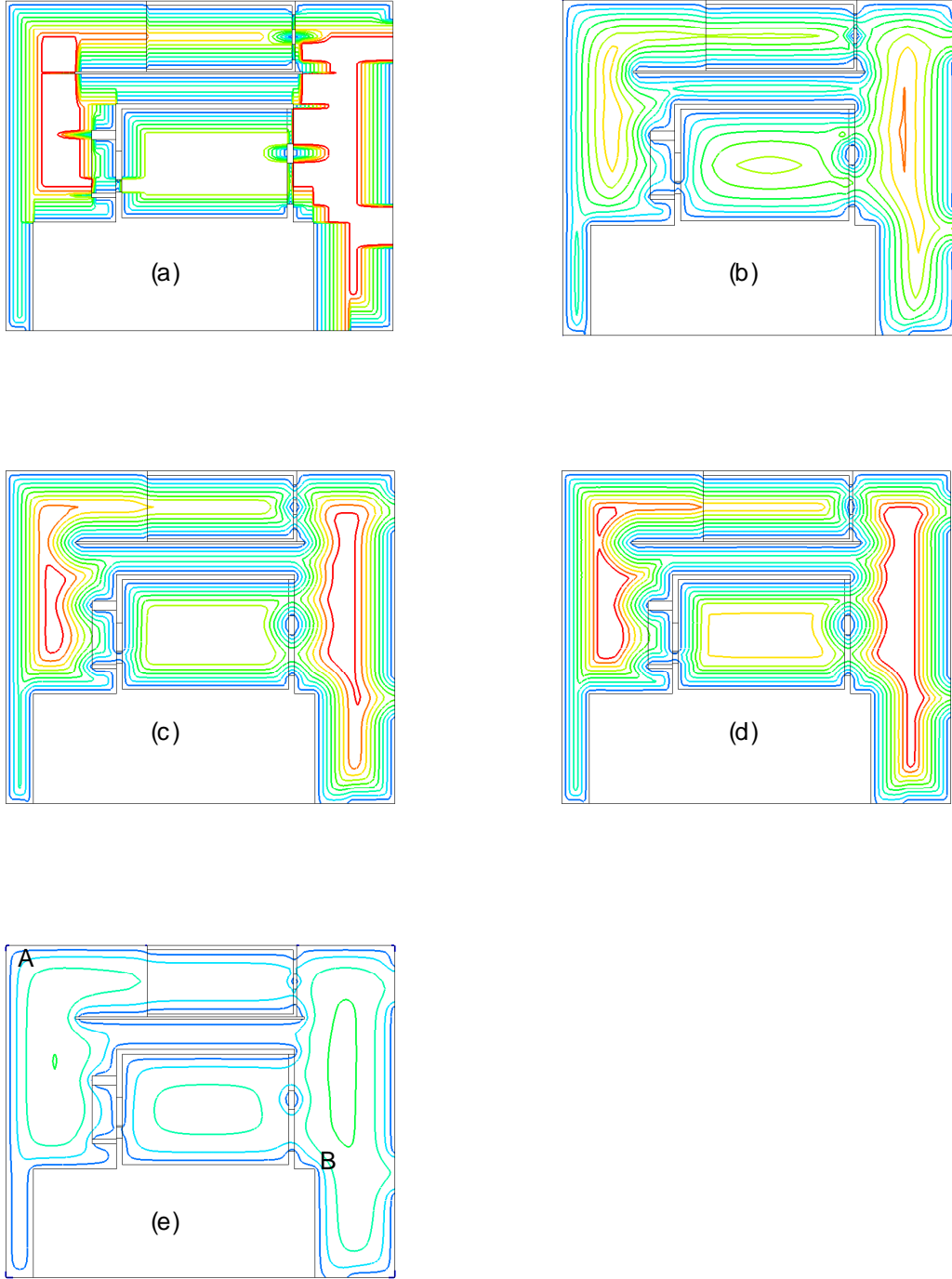
Fig. 11. Case (b) contours of d in the x-y plane for the following approaches: (a) Search (NNS); (b) Poisson; (c) Eikonal; (d) advective; and (e) advection-diffusion.

(a)

(b)
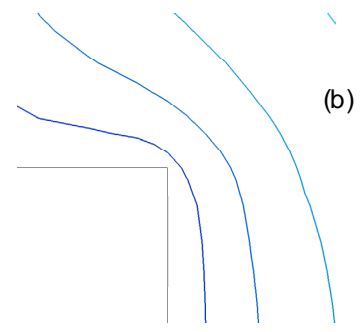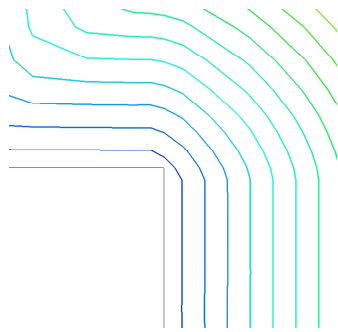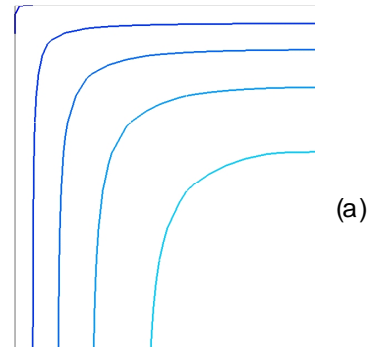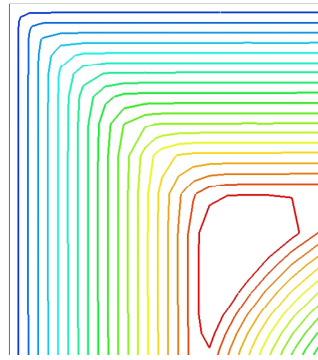
No-Laplacian

Laplacian

Fig. 12. Case (a), influence of Laplacian: (a) Region A and (b) Region B.
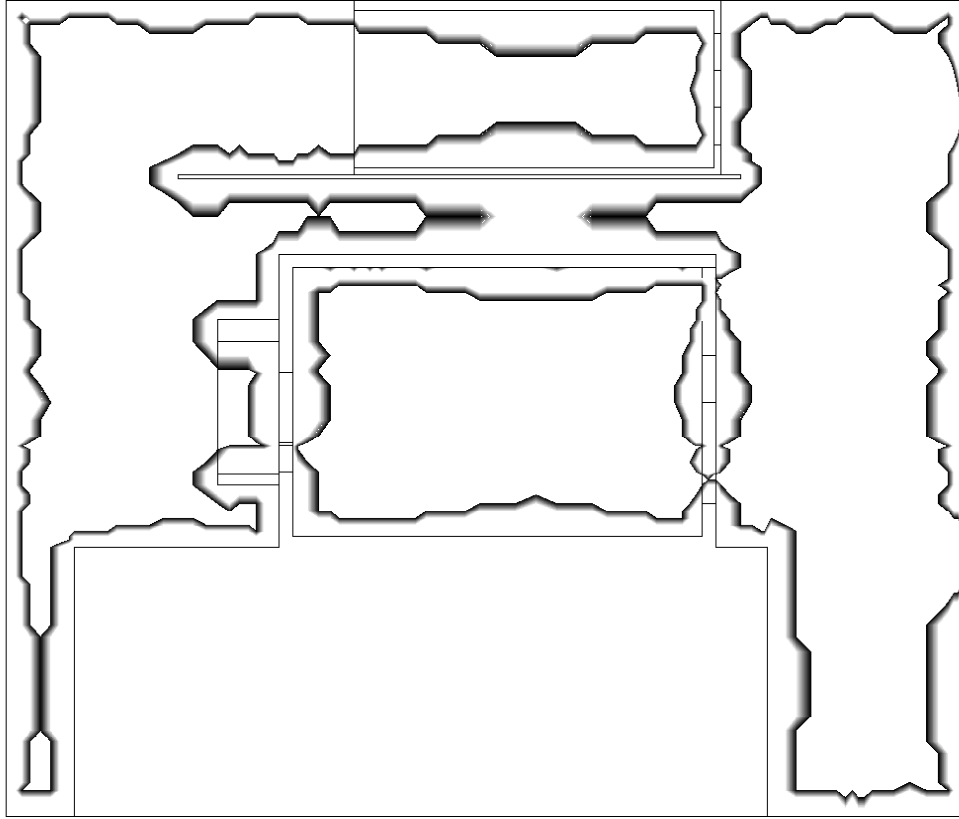
Fig. 13. Case (b) (electronics system) RANS/LES interface for a DES solution using the advective d equation with the MF approach.
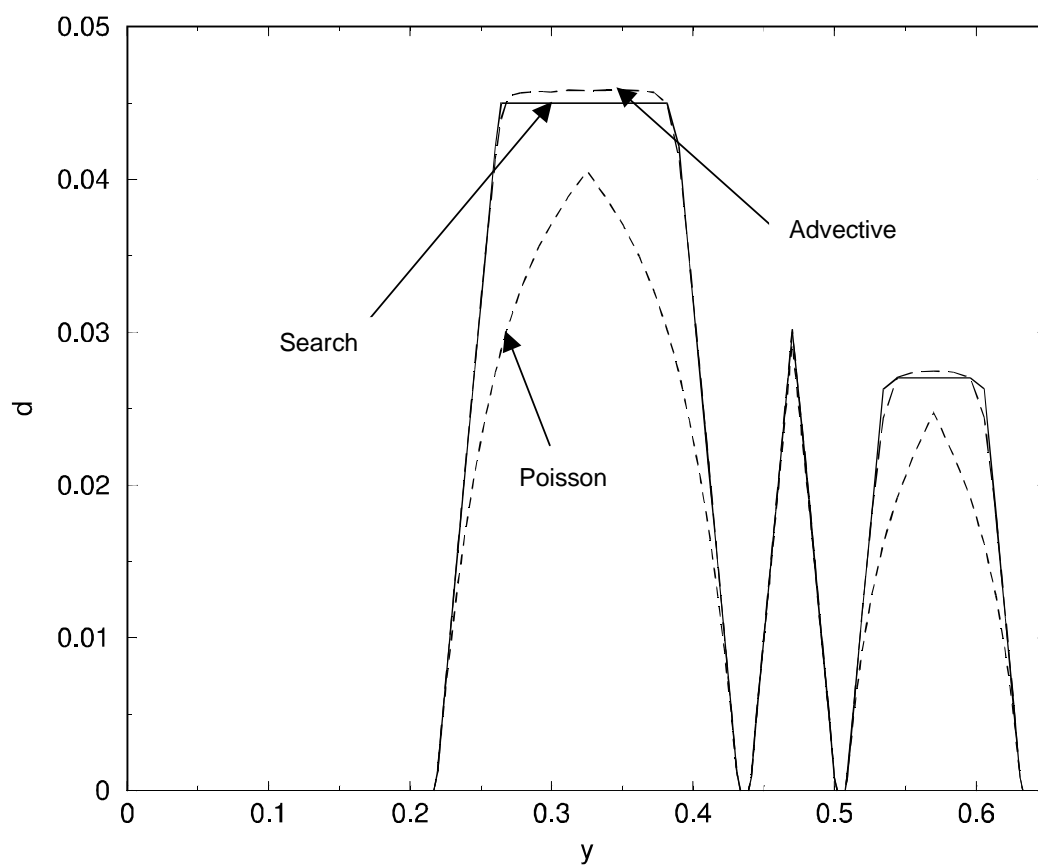
Fig. 14. Case (b) plot of *d* against *y*.
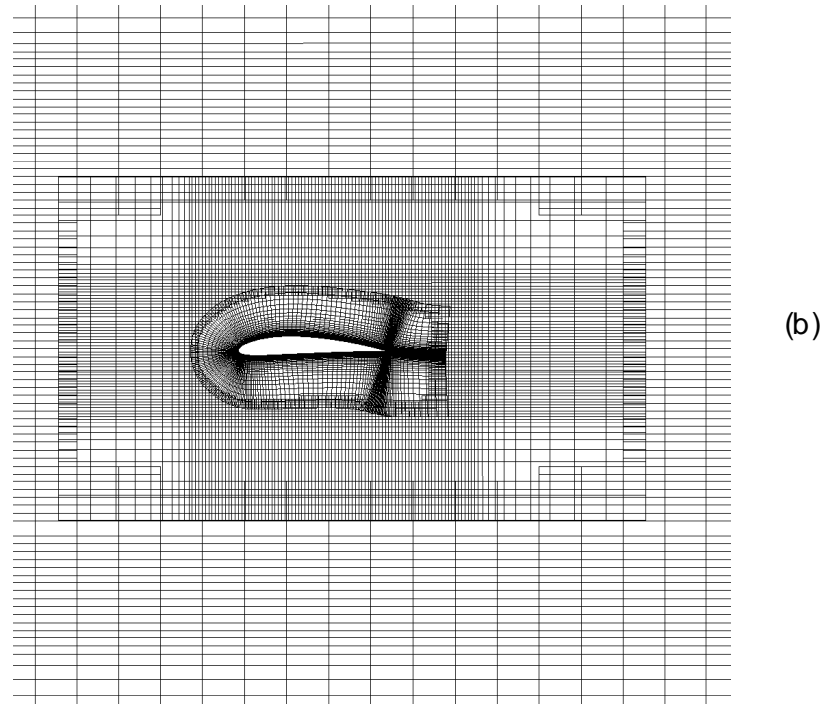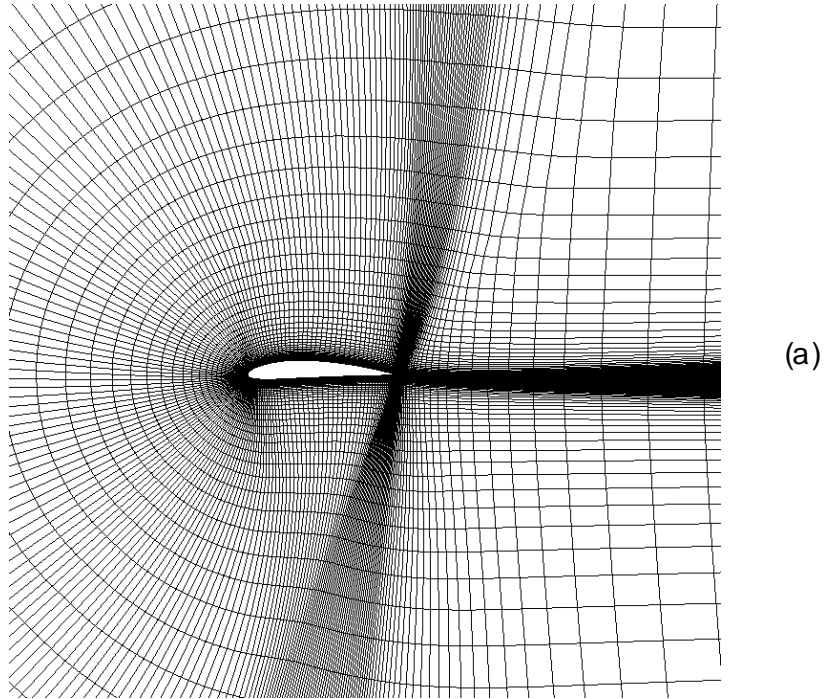
Fig. 15. Case (c) (NACA 4412) grids: (a) single block 'C' and (b) 3-zone overset.
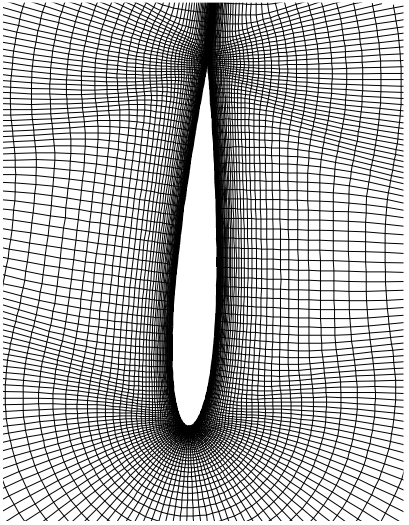
(a)
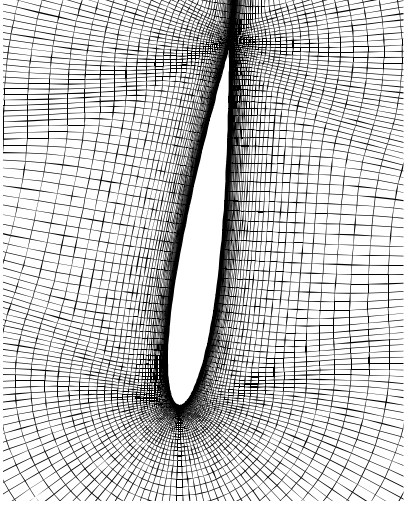
(b)

Fig. 16. Case (c) (NACA 0012) 'C' grids at around: (a) the minimum (2.6°) and (b) maximum (7.2°) pitch angles.

37
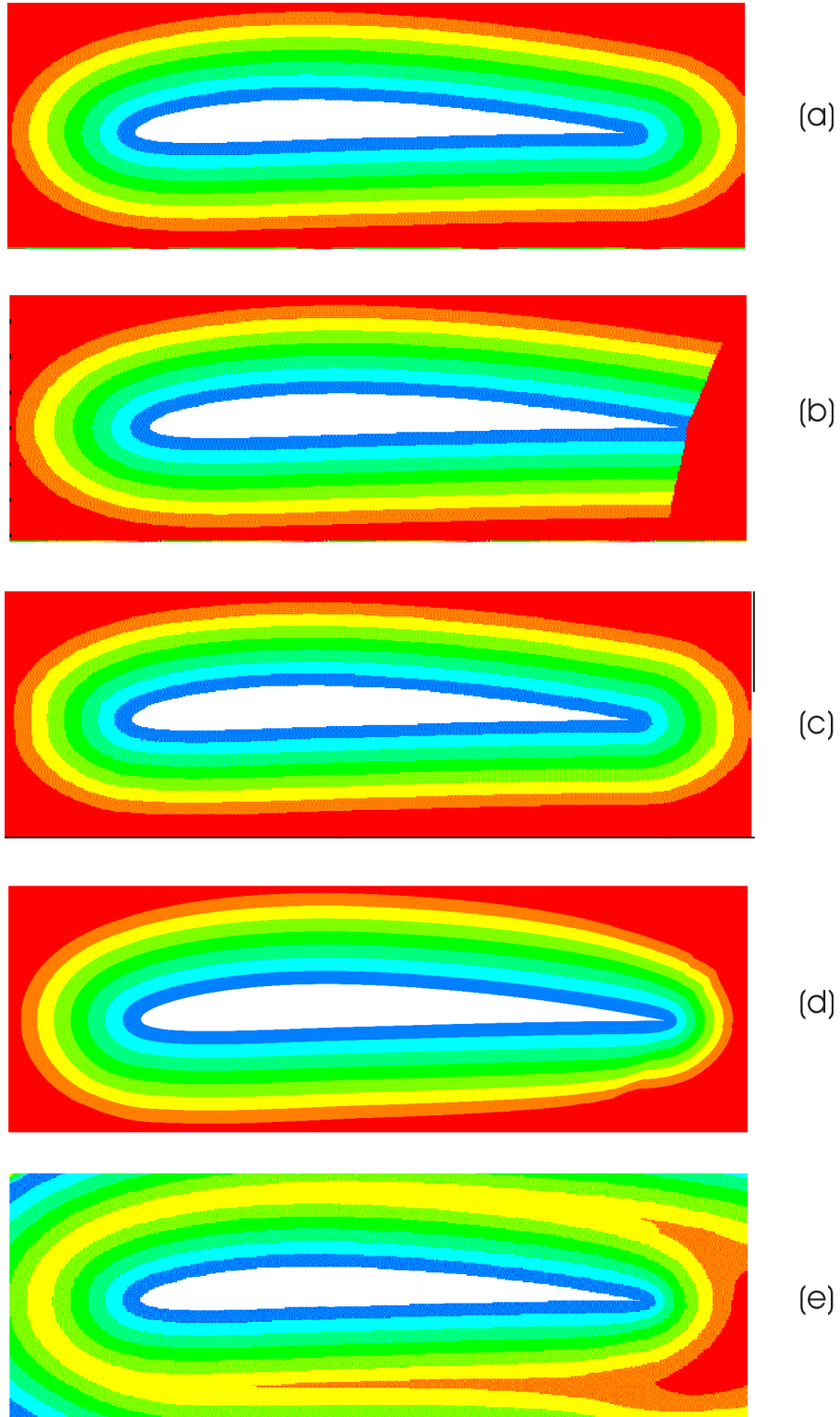
Fig. 17. Case (c) (NACA 4412) d contours: (a) NSS; (b) NNS; (c) advective equation; (d) Poisson and (e) overset grid Poisson.
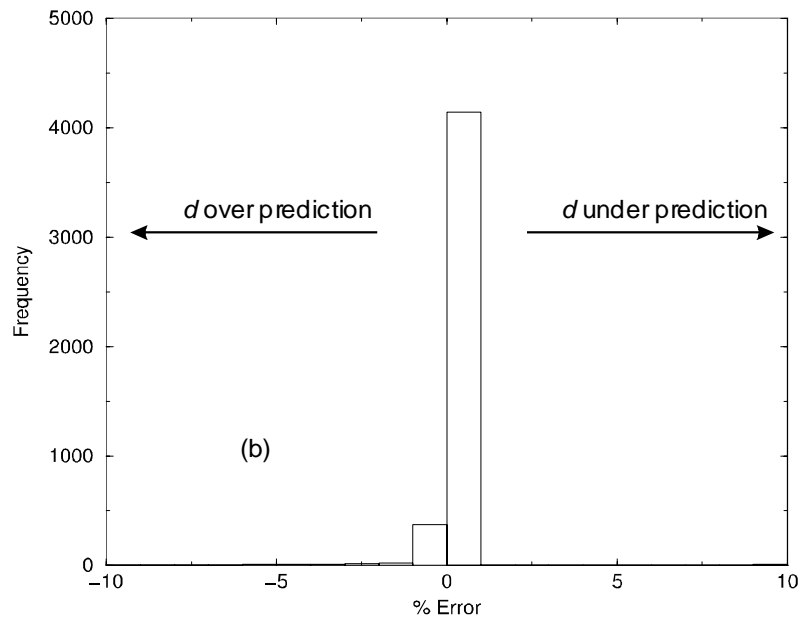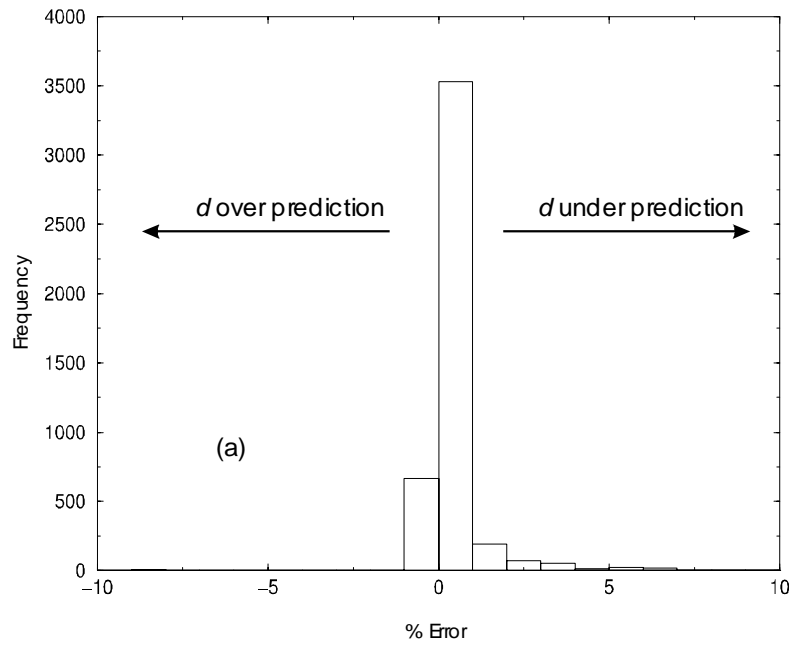
Fig 18. Case (c) (NACA 4412) $y^+ < 400$ Error histogram: (a) advective d equation and (b) Poisson.
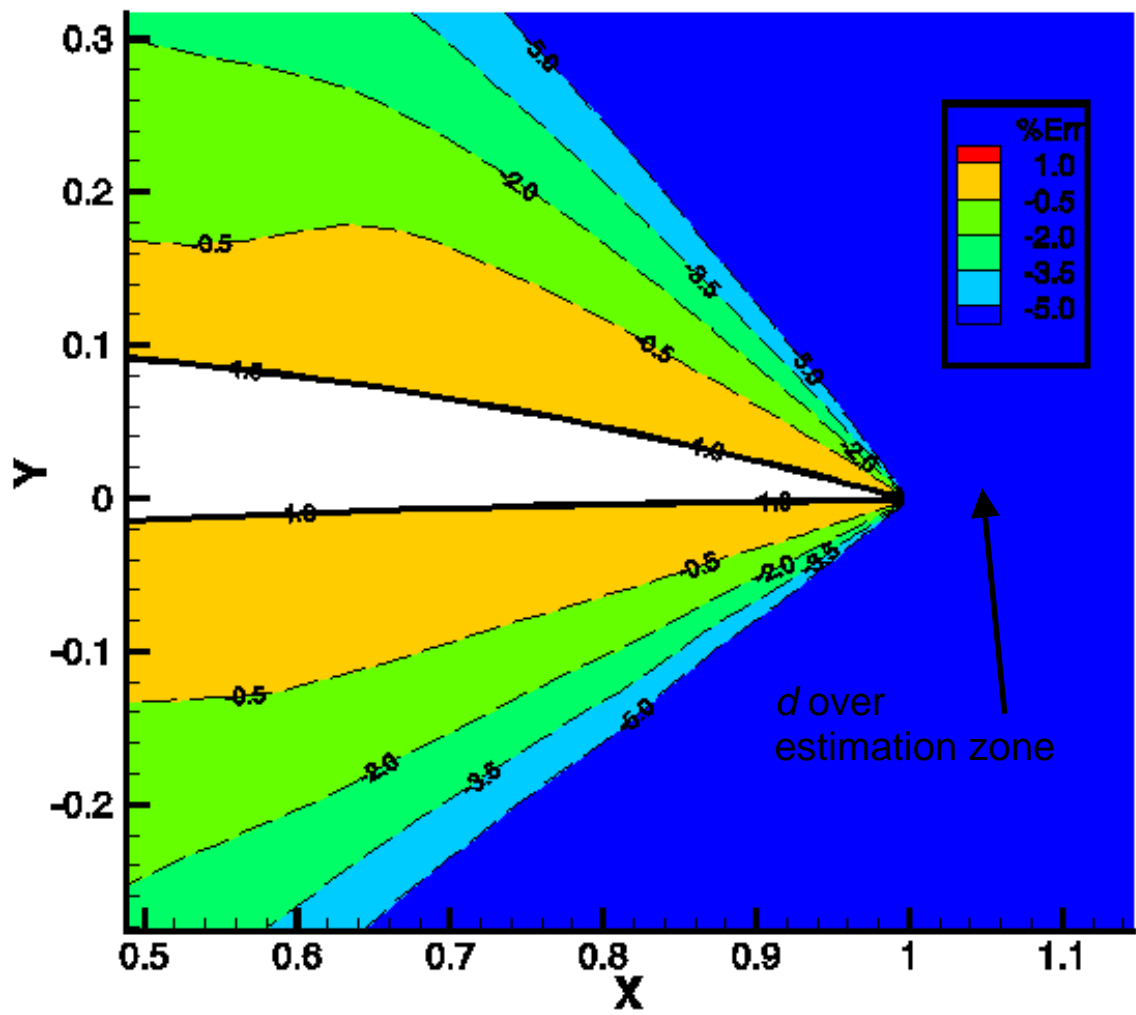
Fig. 19. Case (c) (NACA 4412) Poisson d 'error' contours.
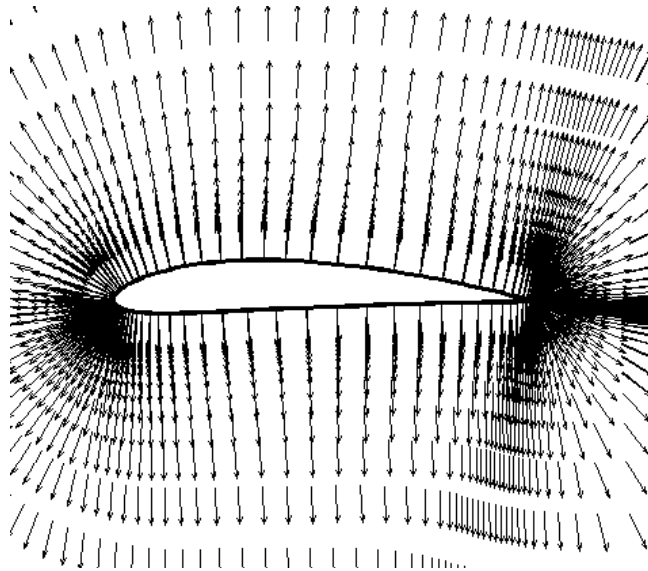
(a)
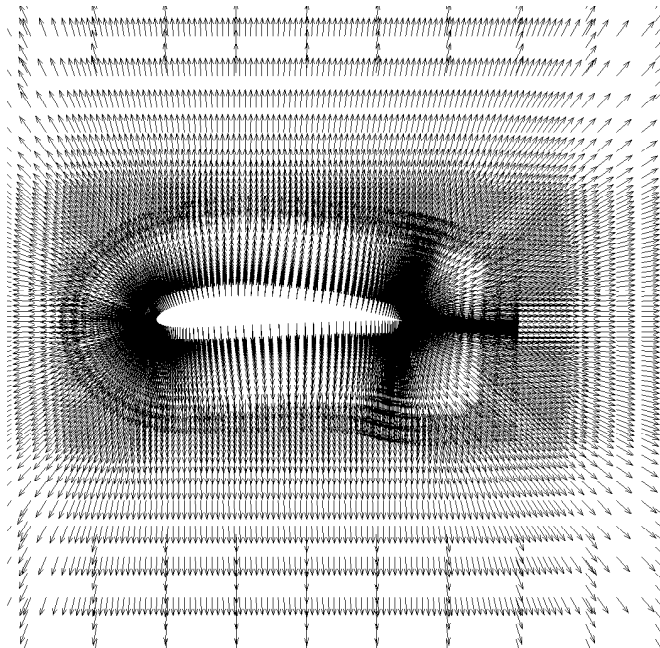
(b)

Fig. 20. Case (c) (NACA 4412) **U** vectors for the advective d equation: (a) 'C' grid;
(b) overset grid.
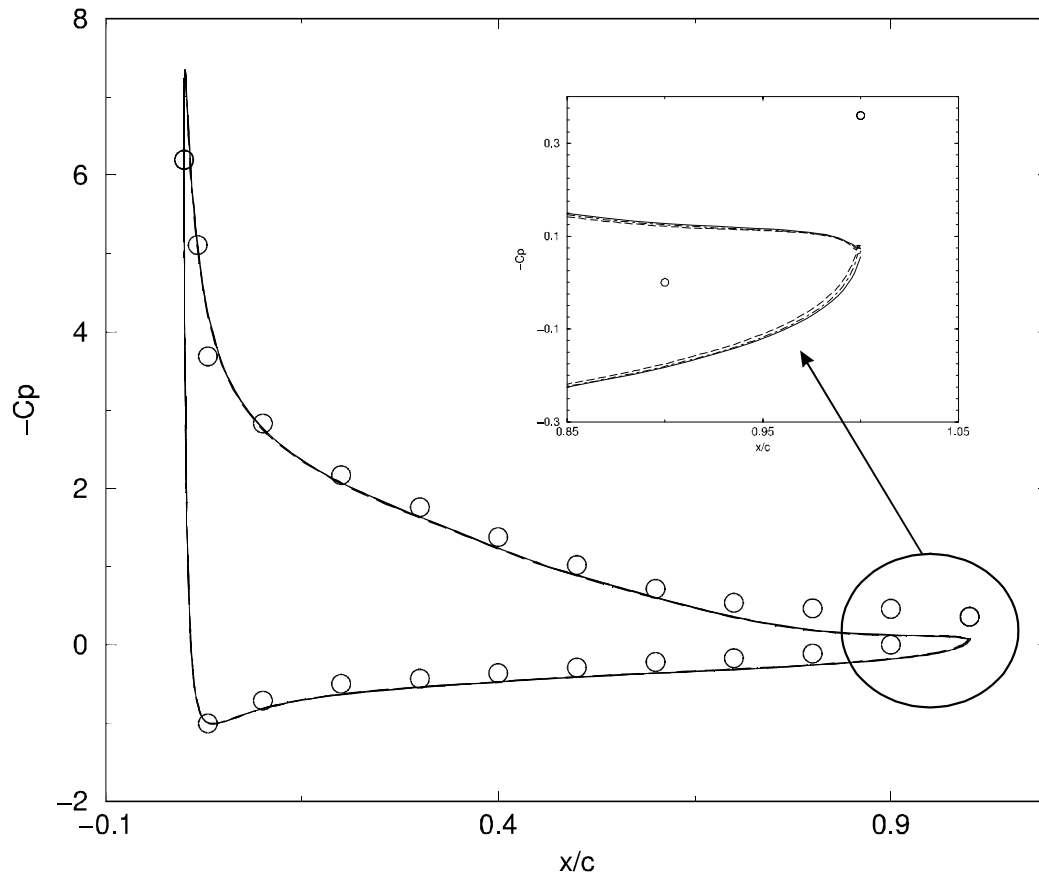
Fig. 21. Case (c) NACA4412 surface *Cp* plots
(O measurements, —— Poisson, - - - -NSS, -··-··- NNS approaches)
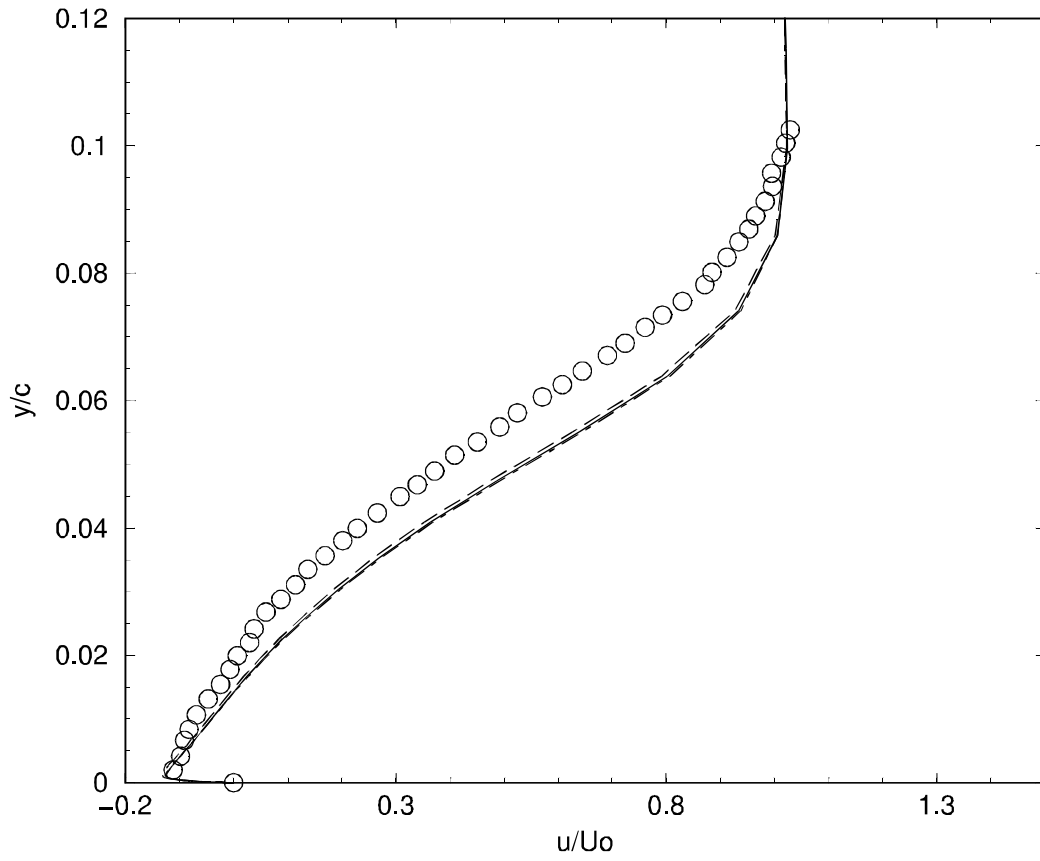
Fig. 22. Case (c) (NACA4412) streamwise fluid velocity against the cross-stream coordinate near the trailing edge at *x/c* = 0.953 (O measurements, —— Poisson, - - - -NSS, . _._ ._ ._ . NNS approaches)
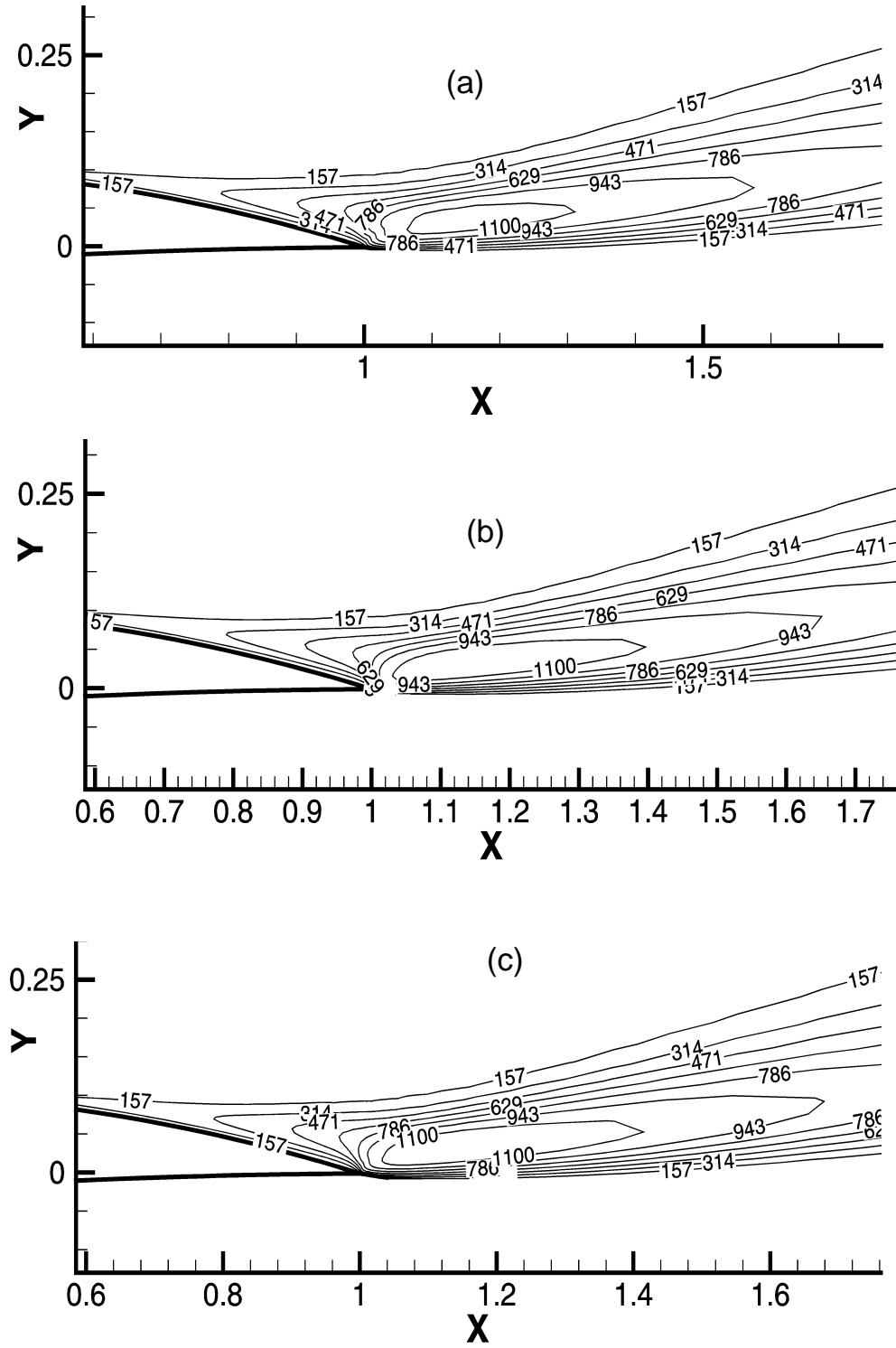
Fig. 23. Case (c) (NACA 4412) turbulent viscosity contours for the following *d* fields :
(a) NSS; (b) NNS and (c) Poisson.

Fig. 24. Case (c) (NACA4412) Reynolds stress contours: (a) streamwise normal component, (b) shear component and (c) cross-stream normal component.
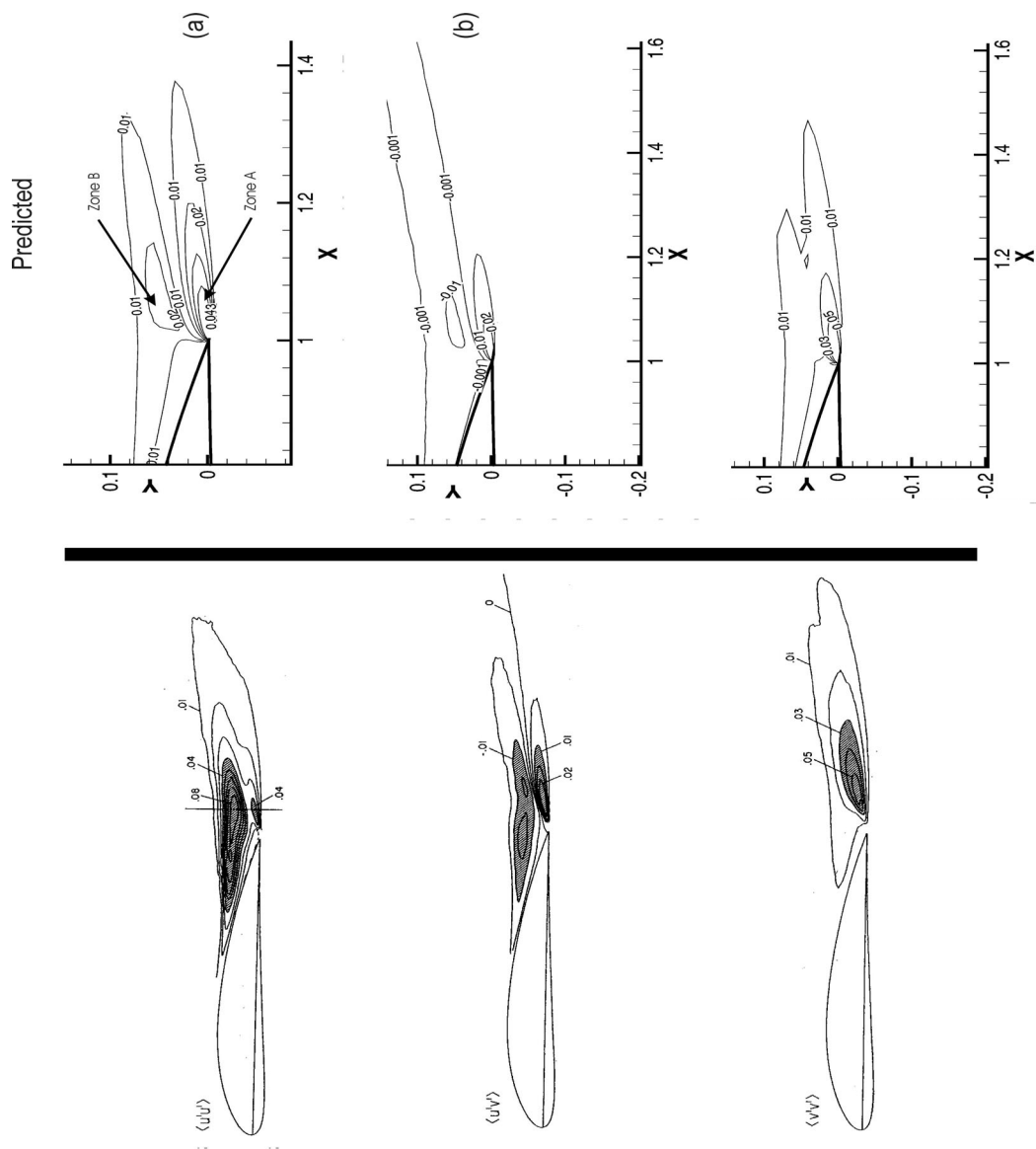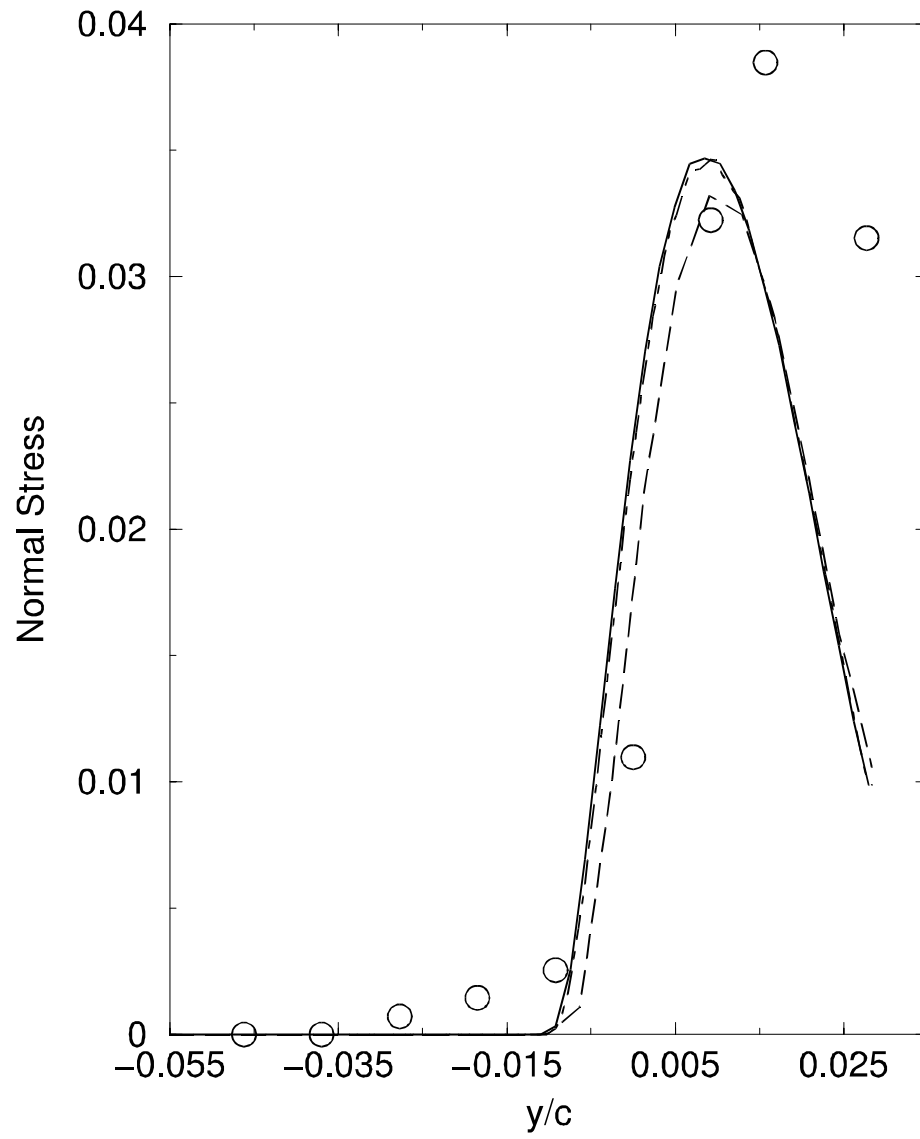
Fig. 25. Case (c) plot of normal stress against *y/c*.
(O measurements, ——Poisson, - - - -NSS, . _ . _ . NNS)
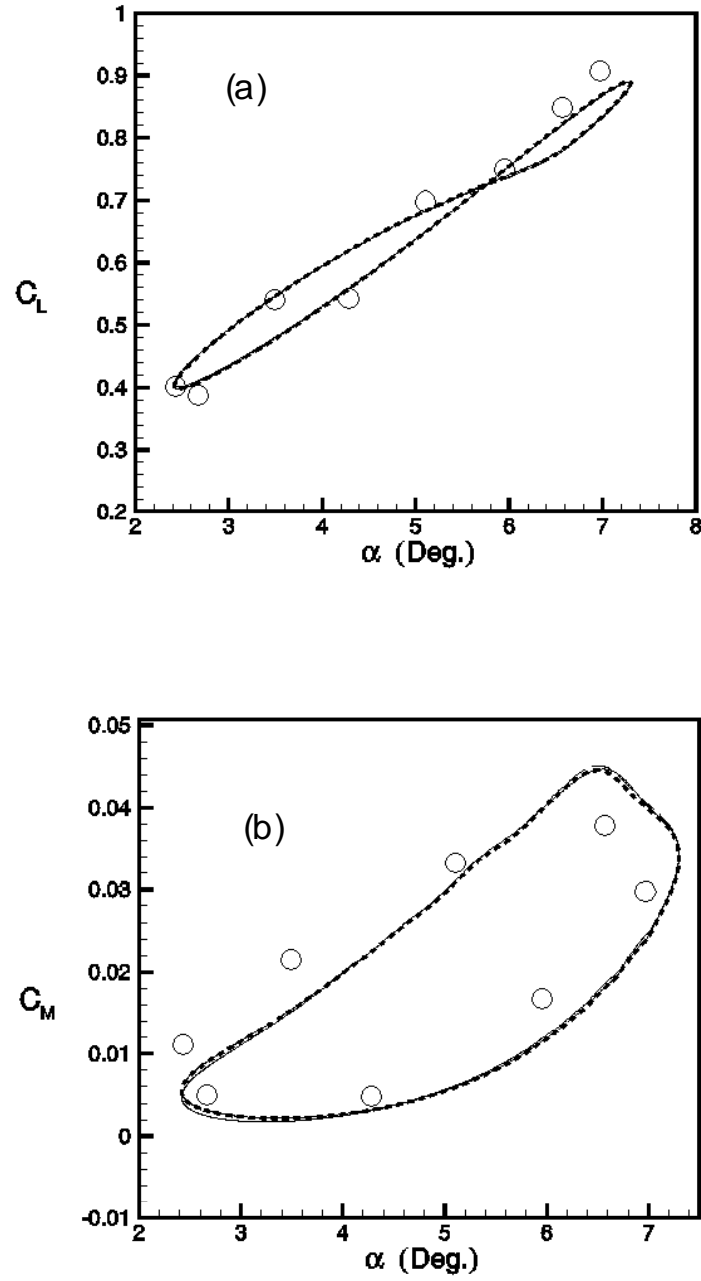
Fig. 26. Case (c) (NACA0012) pitching wing results: (a) lift coefficient variations and (b) moment coefficient variations. (O measurements, ___ non-deforming grid, _ _ _ deforming grid with NSS, ... deforming grid with Poisson)
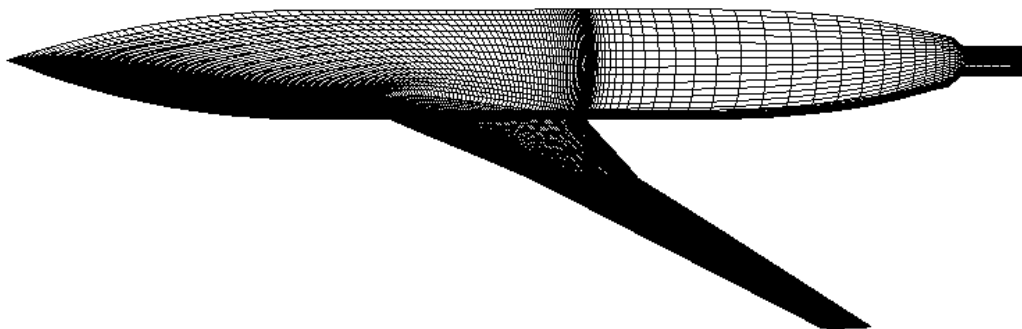
Fig. 27. Case (d) (wing body) grid.
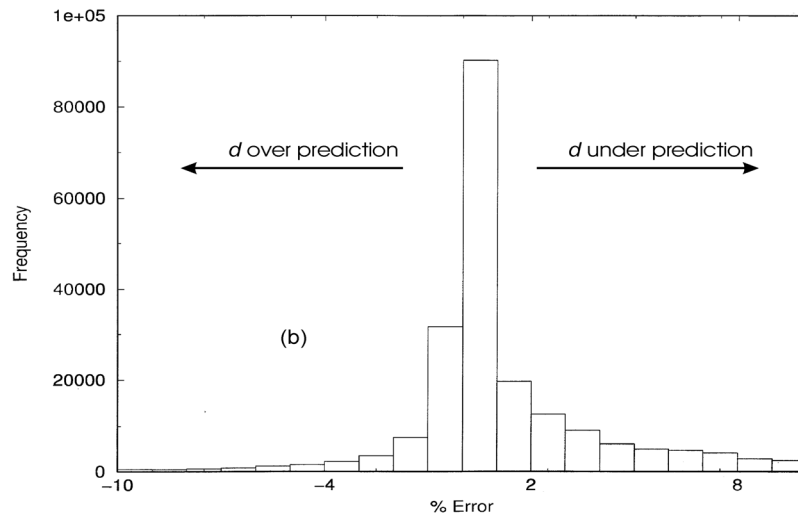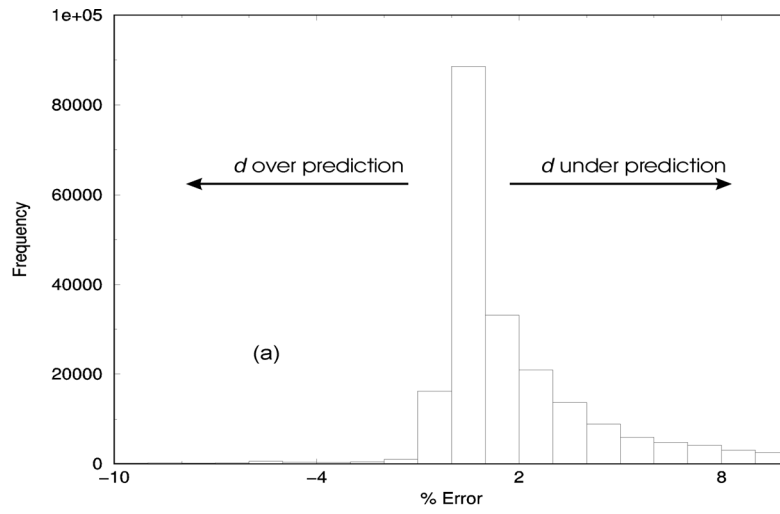
Fig. 28. Case (d) (wing body) $y^+ < 400$ d error histogram: (a) advective equation and (b) Poisson.
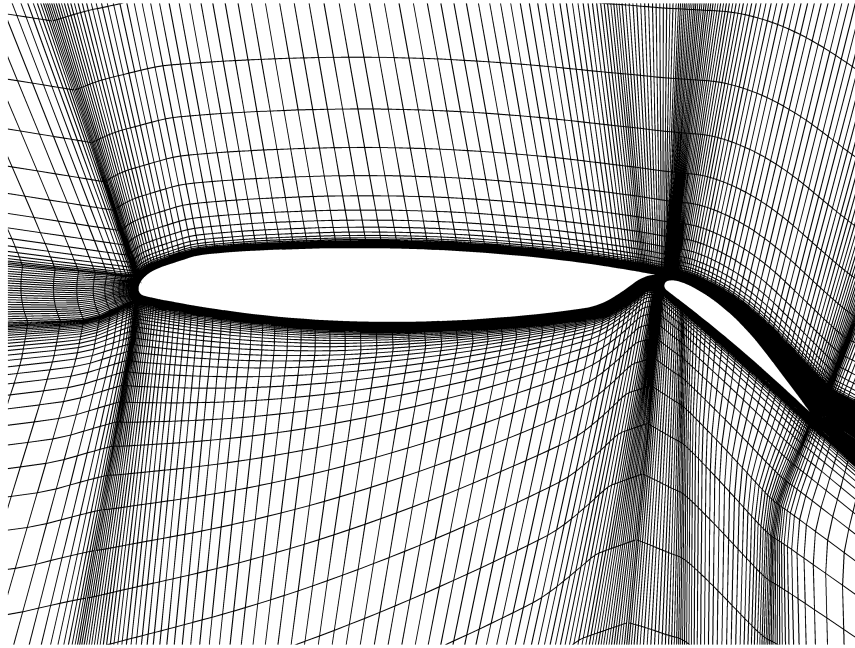
Fig. 29. Case (e) (wing flap) grid.
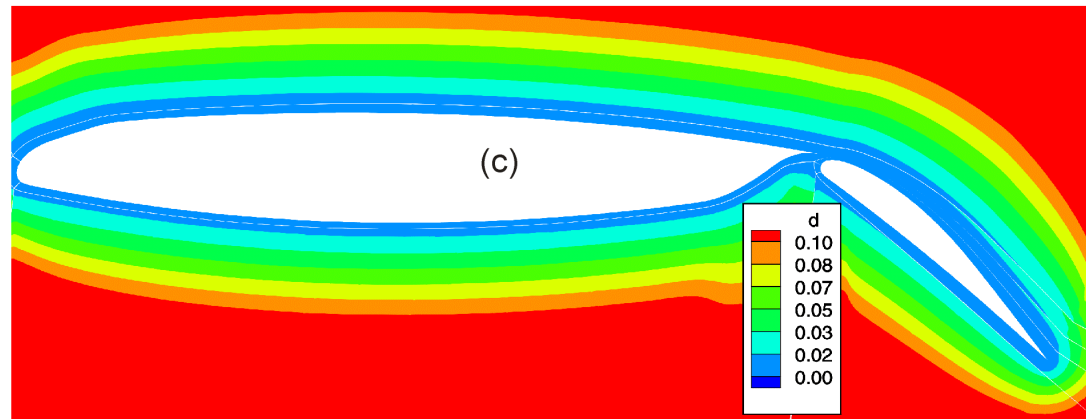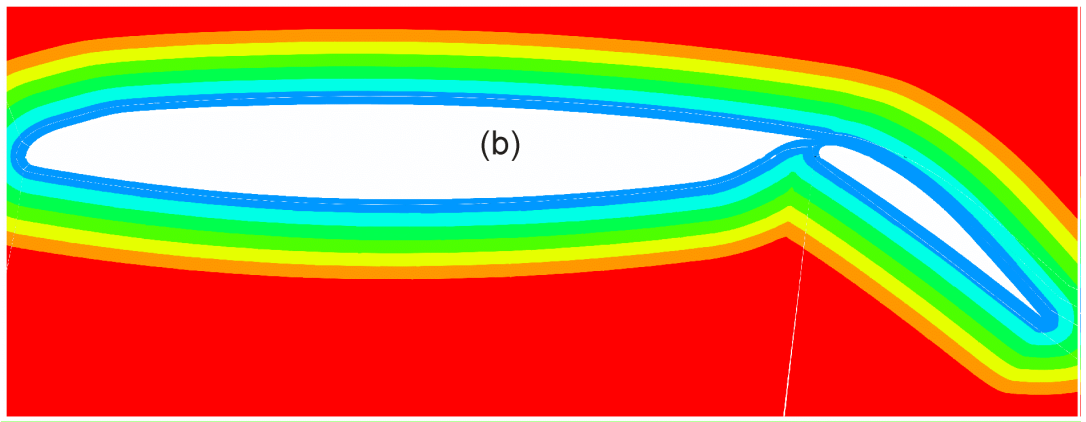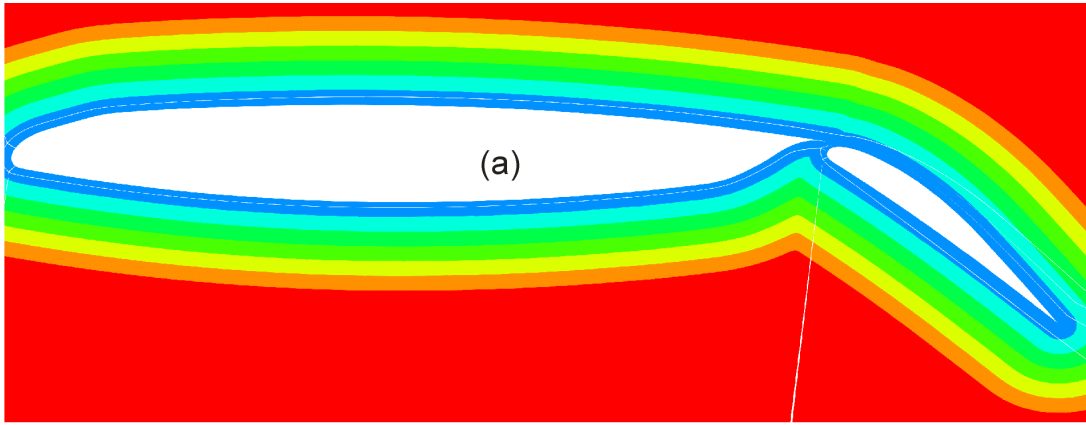
Fig. 30. Case (e) (wing flap) comparison of *d* contours: (a) search (NSS); (b) advective; and (c) Poisson.
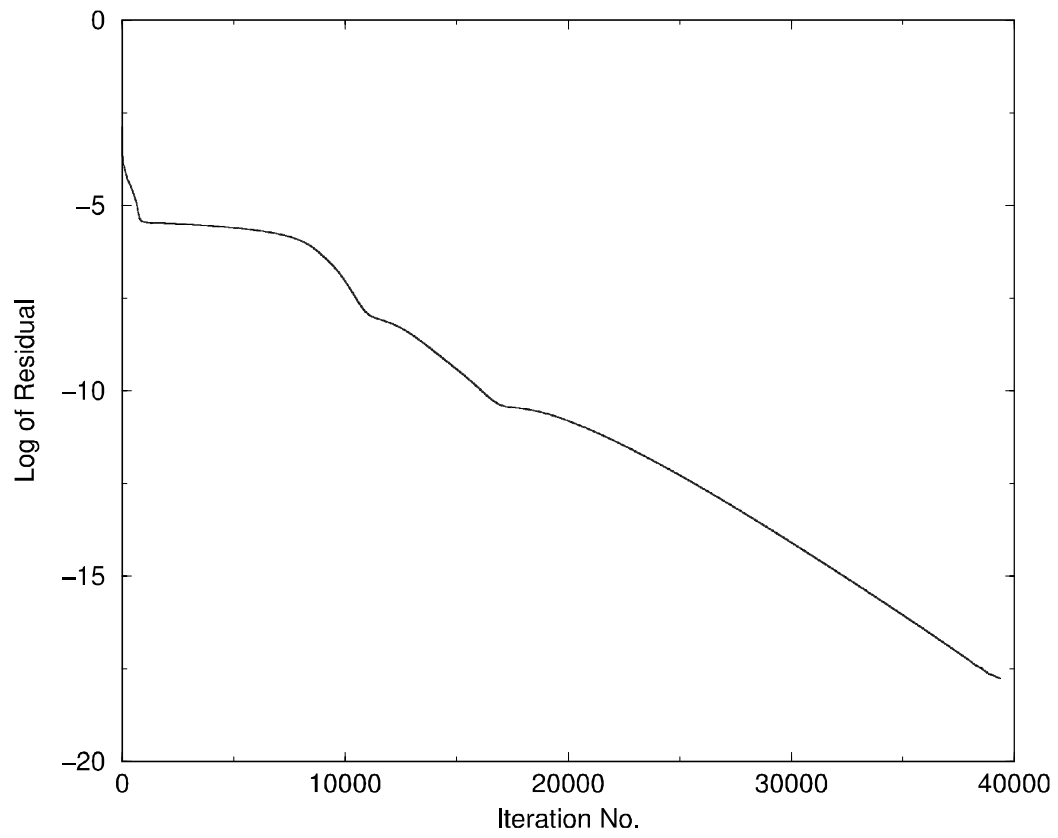
Fig. 31. Case (e) wing-flap GGS convergence history plot.
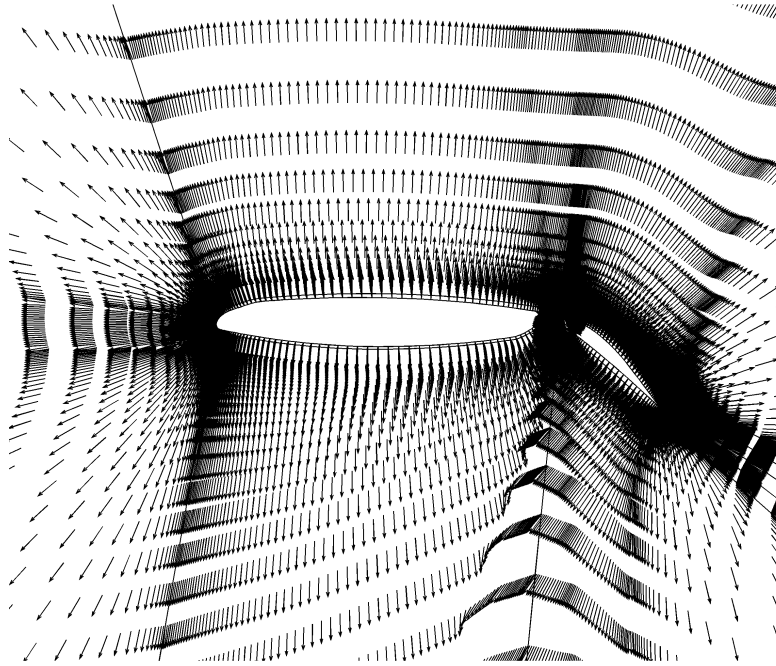
(a)
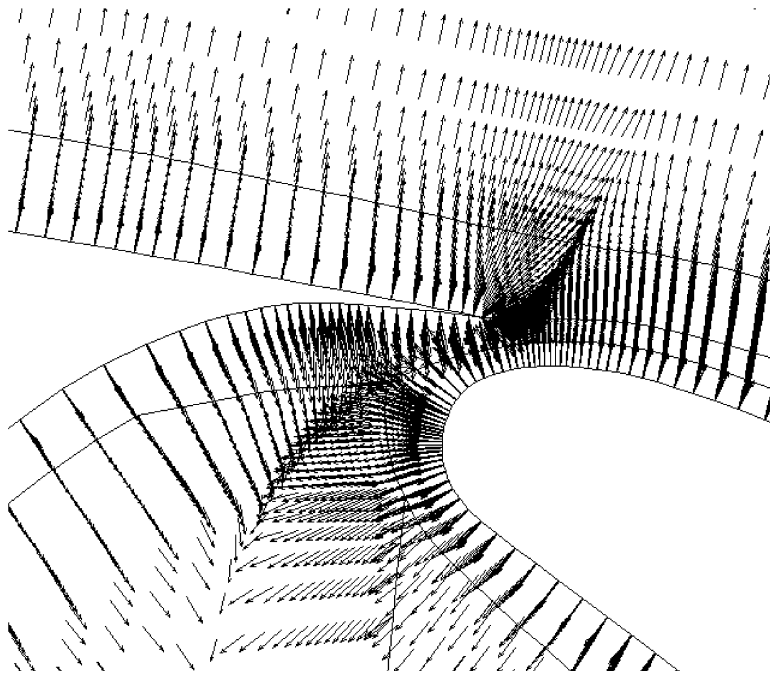
(b)

Fig. 32. Case (e) (wing flap) **U** vectors for the advective equation *d* solution: (a) general view and (b) zoomed-in view.
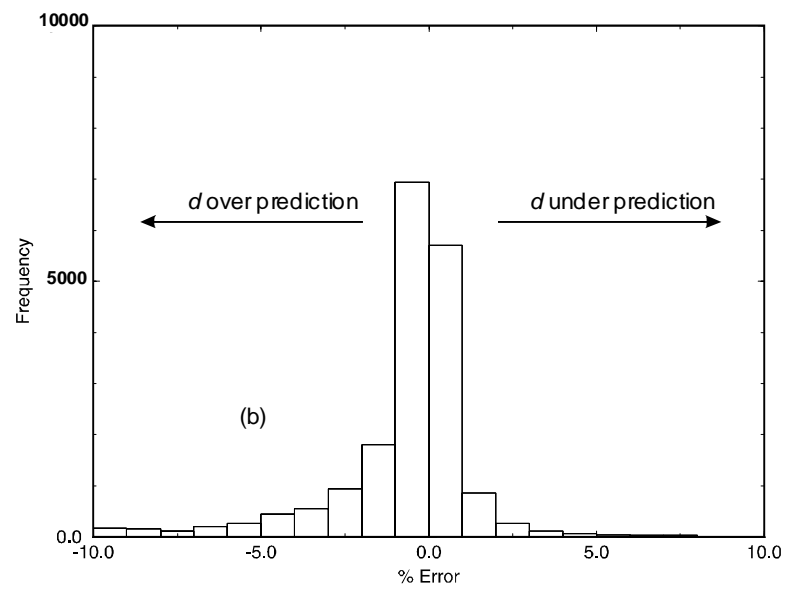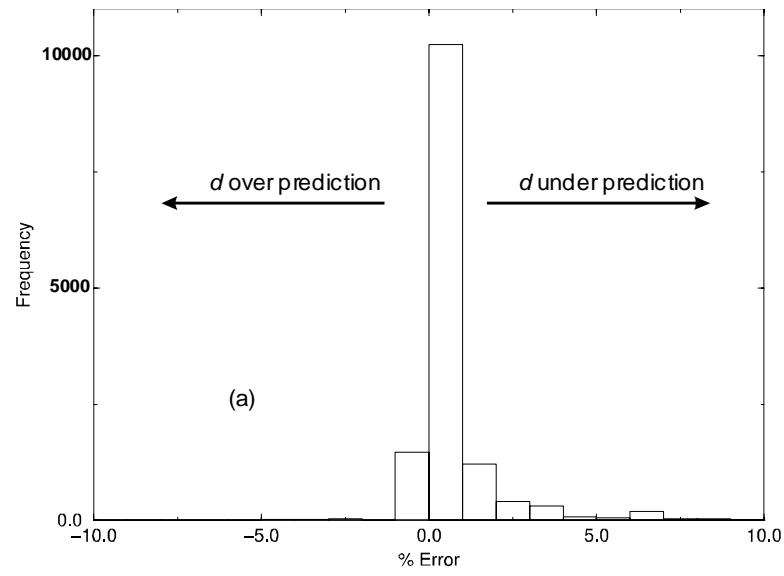
Fig. 33. Case (e) (wing flap) $y^{'} < 400$ d error histogram: (a) advective equation and (b) Poisson.

(a)

(b)

(c)

(d)
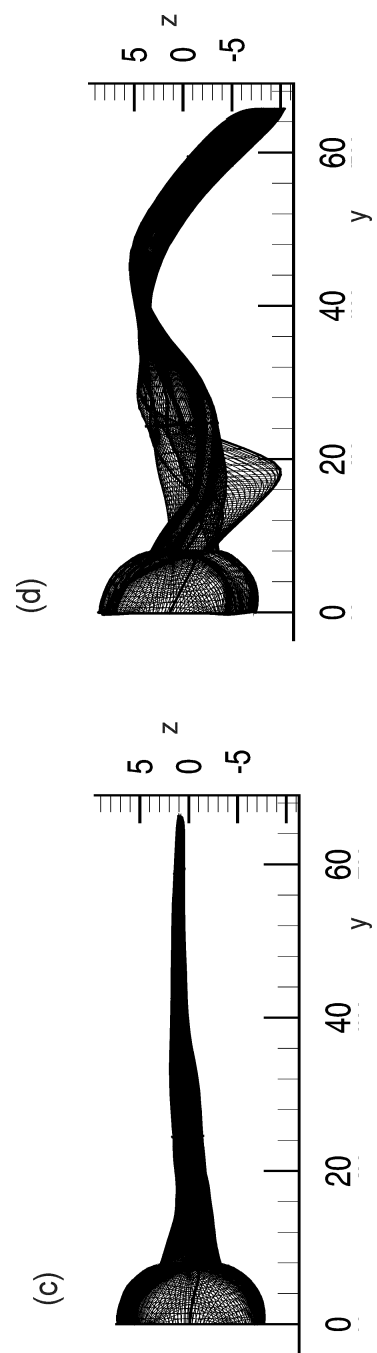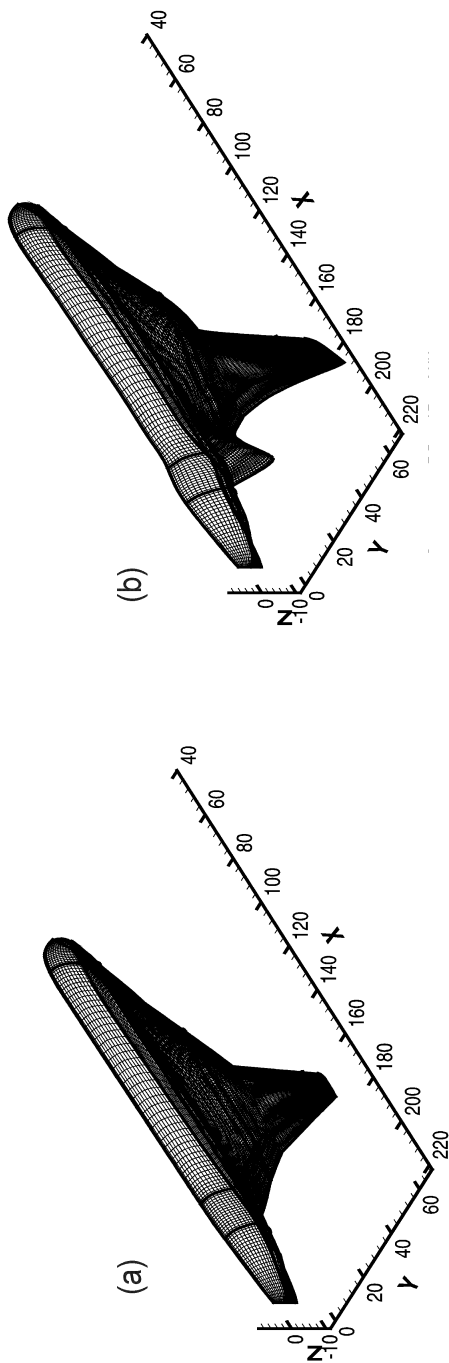
Fig. 34. Case (f) (double delta) initial and fully deformed surface grids: (a,b) 3D views and (c,d) 2D y-z plane views.
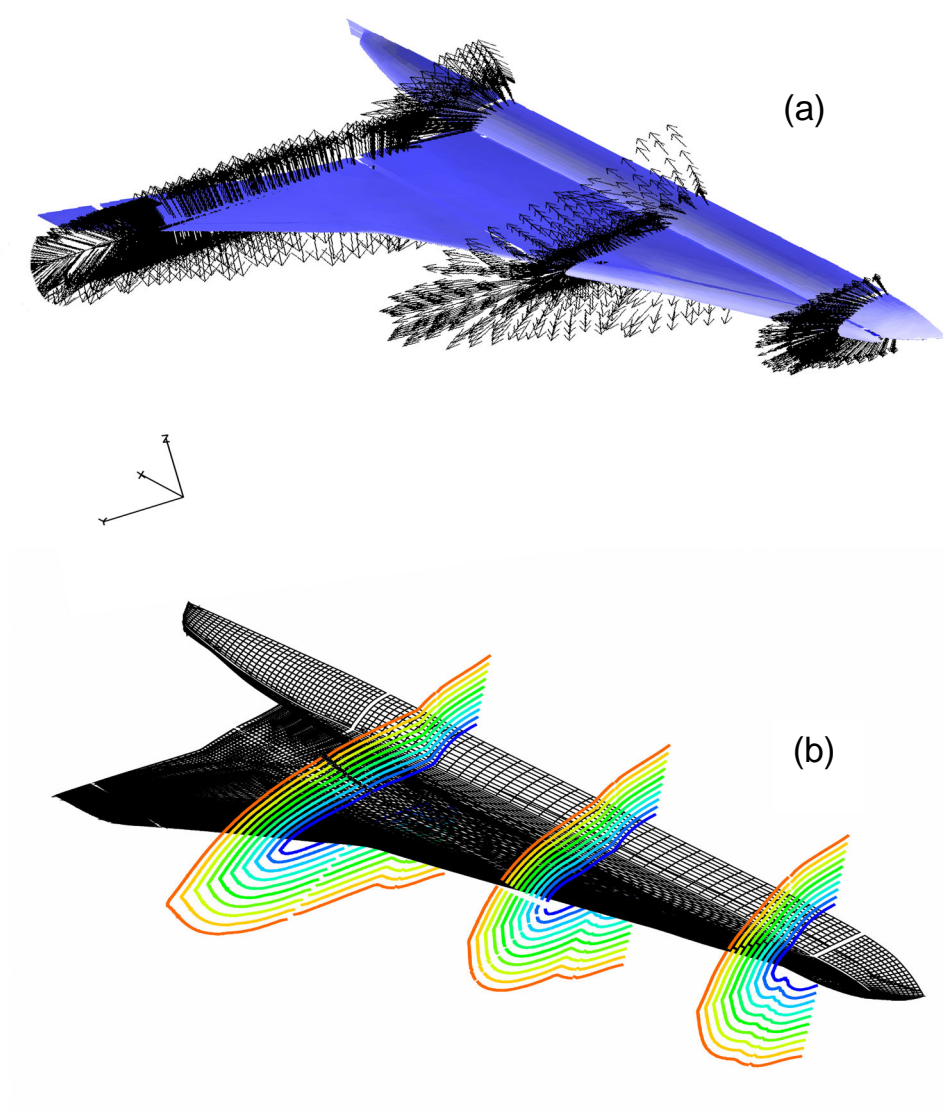
Fig. 35. Case (f) (double delta) advective d equation results in three z-y planes: (a) **U** vectors and (b) d contours.
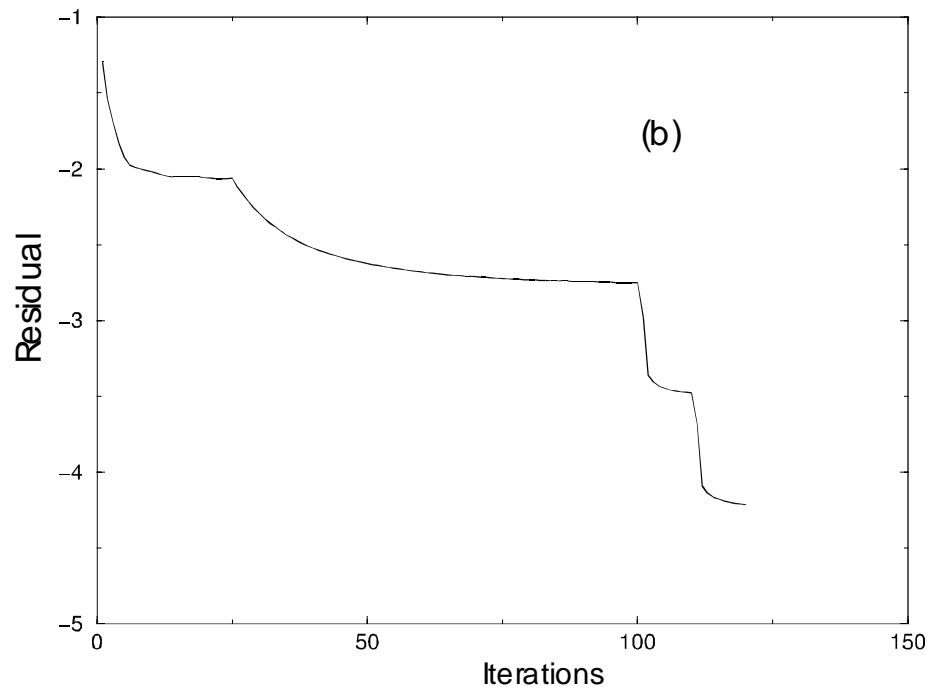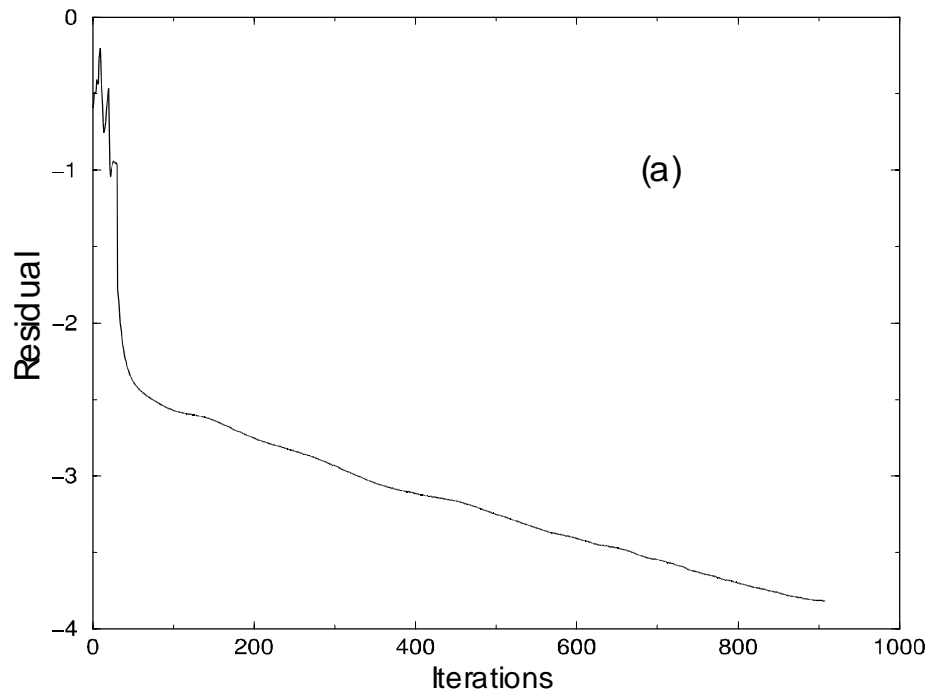
Fig. 36. Case (f) (double delta) residual drops against iteration for
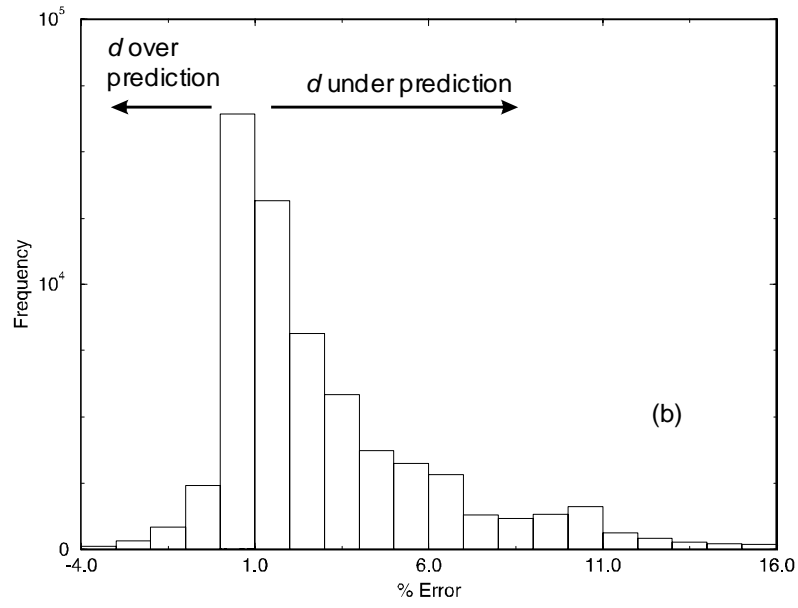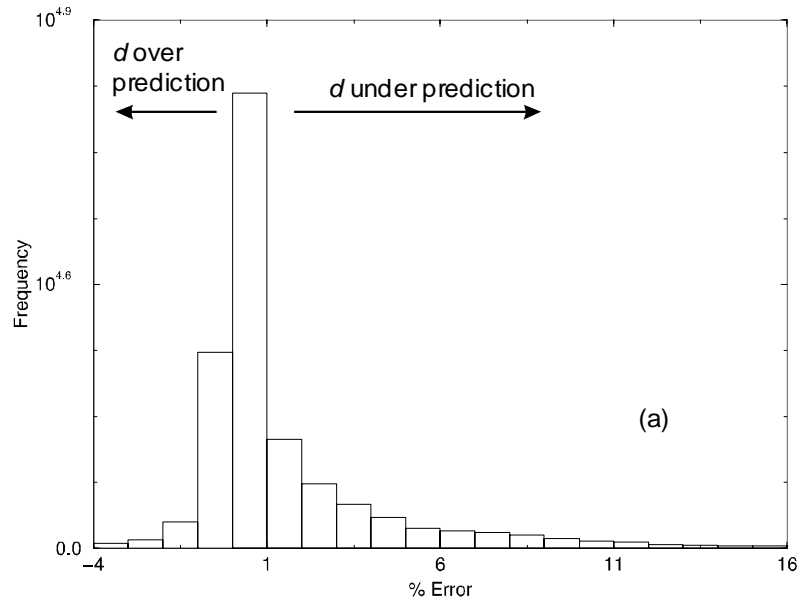stationary mesh solutions: (a) advective equation and (b) Poisson.

Fig. 37. Case (f) (double delta) y < 400d error histogram: (a) advective equation and (b) Poisson.

1. REPORT DATE (DD-MM-YYYY)	2. REPORT TYPE	3. DATES COVERED (From - To)
01- 12 - 2003	Technical Memorandum	

4. TITLE AND SUBTITLE

Transport Equation Based Wall Distance Computations Aimed at Flows With Time-Dependent Geometry

5a. CONTRACT NUMBER

5b. GRANT NUMBER

5c. PROGRAM ELEMENT NUMBER

6. AUTHOR(S)

Tucker, Paul G.; Rumsey, Christopher L.; Bartels, Robert E.; and Biedron, Robert T.

5d. PROJECT NUMBER

5e. TASK NUMBER

5f. WORK UNIT NUMBER

23-719-10-50

7. PERFORMING ORGANIZATION NAME(S) AND ADDRESS(ES)

NASA Langley Research Center
Hampton, VA 23681-2199

8. PERFORMING ORGANIZATION REPORT NUMBER

L-18339

9. SPONSORING/MONITORING AGENCY NAME(S) AND ADDRESS(ES)

National Aeronautics and Space Administration
Washington, DC 20546-0001

10. SPONSOR/MONITOR'S ACRONYM(S)

NASA

11. SPONSOR/MONITOR'S REPORT NUMBER(S)

NASA/TM-2003-212680

12. DISTRIBUTION/AVAILABILITY STATEMENT

Unclassified - Unlimited
Subject Category 02
Availability: NASA CASI (301) 621-0390   Distribution: Nonstandard

13. SUPPLEMENTARY NOTES

Tucker: University of Warwick; Rumsey, Bartels, and Biedron: Langley Research Center
An electronic version can be found at http://techreports.larc.nasa.gov/ltrs/ or http://ntrs.nasa.gov

14. ABSTRACT

Eikonal, Hamilton-Jacobi and Poisson equations can be used for economical nearest wall distance computation and modification. Economical computations may be especially useful for aeroelastic and adaptive grid problems for which the grid deforms, and the nearest wall distance needs to be repeatedly computed. Modifications are directed at remedying turbulence model defects. For complex grid structures, implementation of the Eikonal and Hamilton-Jacobi approaches is not straightforward. This prohibits their use in industrial CFD solvers. However, both the Eikonal and Hamilton-Jacobi equations can be written in advection and advection-diffusion forms, respectively. These, like the Poisson's Laplacian, are commonly occurring industrial CFD solver elements. Use of the NASA CFL3D code to solve the Eikonal and Hamilton-Jacobi equations in advective-based forms is explored. The advection-based distance equations are found to have robust convergence. Geometries studied include single and two element airfoils, wing body and double delta configurations along with a complex electronics system. It is shown that for Eikonal accuracy, upwind metric differences are required. The Poisson approach is found effective and, since it does not require offset metric evaluations, easiest to implement. The sensitivity of flow solutions to wall distance assumptions is explored. Generally, results are not greatly affected by wall distance traits.

15. SUBJECT TERMS

Wall distance; Non-stationary grids; Turbulence; Computational aeroelasticity

16. SECURITY CLASSIFICATION OF:			17. LIMITATION OF ABSTRACT	18. NUMBER OF PAGES	19a. NAME OF RESPONSIBLE PERSON
a. REPORT	b. ABSTRACT	c. THIS PAGE			STI Help Desk (email: help@sti.nasa.gov)
U	U	U	UU	67	19b. TELEPHONE NUMBER (Include area code) (301) 621-0390